Title: Spatial anchor of adaptive immune cell around biomaterials mediated large-scale wound regeneration

Authors: Yang Yang[1]†, Chen-yu Chu[1]†, Li Liu[1], Chen-bing Wang[1], Chen Hu[1], Xin-hui Li[1], Yi-li Qu[1]*, Yi Man[1]*

Affiliations:

[1] Department of Oral Implantology &State Key Laboratory of Oral Diseases & National Clinical Research Center for Oral Diseases, West China Hospital of Stomatology, Sichuan University; Chengdu 610041, China.

* Corresponding author. Email: manyi780203@126.com (Y.M.); qqyili@126.com (Y.L.Q.)

† These authors contributed equally to this work

Abstract: Generally, only few HF (hair follicle) can regenerate upon severe wound in adult mammals, which restricted in the large wound center, termed wound-induced hair follicle neogenesis (WIHN). Integration the gene expression profiles of spatial transcriptomic (ST) and Single-cell RNA sequencing (scRNA-seq) highlighted the preferential aggregation of adaptive immune cells in the large wound center co-localizing with HF precursor cells. Further we observed that wound recapitulated normal skin architecture with the implantation of extracellular matrix (ECM) scaffolds regardless of wound size. Enlarged distribution of the adaptive immune cells around biomaterials, overlapping with HF precursor cells, may account for the enhanced WIHN in biomaterial-implanted wound. Loss the capacity of WIHN in Rag2$^{-/-}$ mice validated the potential therapeutic effect of manipulating adaptive immune system for the scar-less wound regeneration.

One-Sentence Summary: Multimodal analysis predicted the regenerative effect of adaptive immune system activated by biomaterial during wound healing

Main Text:

Large fibrotic scar devoid of skin appendages seriously affect the patient's daily life, which is one of the primary impediments to wound healing(*1*). ECM scaffolds are one of the efficient treatments for severe wound (*2*) but still lacking ability of stimulating HF neogenesis(*3*). Intriguingly, rare capacity of HF regeneration has been observed in large full-thickness wound

center in WIHN model(*4, 5*). It has been suggested that immune cells (mainly macrophages, T cells) might be the key orchestrators of wound healing that selectively promoting scarring(*6-8*) or regenerative WIHN(*9-12*), while the spatial heterogeneity of immune systems still unclear. Biological cues can be integrated into polymer scaffold to create a mimic of the native ECM, which is the framework guiding the activity of immune cells (*13, 14*). Our previous study has showed that the ECM scaffold was able to lead to an enhanced regeneration of HF along with the immunomodulatory effect (*15, 16*). However, the foreign body response (FBR) triggered by biomaterials and the specific immunomodulatory effect on cutaneous cells remains elusive. In this study, we firstly repeated the WIHN phenomenon in large area (diameter = 1.5cm) splinted excisional wound healing model, marked by de novo HF regeneration restricted in wound center. Next we showed that the ECM scaffold exerts the further pro-regenerative effect on enhanced WIHN despite of wound size. Multiomics approaches including scRNA-seq and ST were applied to delineate the delicate spatial characteristics of immune-microenvironment during wound healing. Integrated analysis highlighted the preferential aggregation of T cell, monocyte, and pro-inflammatory macrophage (PIM) co-localized with the HF precursor cells around scaffold. Abundant local intercellular communications between them suggested the therapeutic potential of adaptive immune system in HF regeneration. Rag2$^{-/-}$ mice which lack the HF regeneration ability provided further evidence that the adaptive immune system activated by biomaterials was crucial in scar-less wound healing.

WIHN occurred in large wound center with activation of adaptive immune system

We created small and large area (diameter from 0.6cm to 1.5cm) circular wound in murine splinted full-thickness excisional wound healing model (Fig. 1A and B). Comparison of de novo HF number among different wound size confirmed the WIHN occurred in large wound (diameter = 1.5cm) center, while small wound (diameter < 1.5cm) healed with the characteristic of fibrotic scar devoid of dermal appendages (Fig. 1C). To explore the underlying mechanism stimulating the WIHN, we respectively created Ctrl_SW (diameter = 0.6cm) and Ctrl_LW (diameter = 1.5cm) group of different wound size and harvested wound tissue for the further examination (Fig. 1D). In comparison with small wound, the large wound showed up-regulated gene expression enriched in hair follicle development and αβT cell differentiation (Fig. 1E). Correlation heatmap showed the positive correlation between HF regeneration related genes and adaptive immune response related genes (Fig. 1 F). Immunofluorescent (IF) staining (Fig. 1G)

and flow cytometry (Fig. 1H) confirmed that large wound (especially wound center) maintained substantial adaptive T cell infiltration.

Integration of spatial transcriptomics and scRNA-seq profiling

To explore the spatial characteristic of single cells during wound healing, we applied the ST and scRNA-seq to analyze spatial gene expression profiles of small and large wound (Fig. 2A and fig. S1). Based on ST profile, the anatomical structure of the wounds could be clearly distinguished (Fig. 2B). Gene enrichment analysis showed that the Ctrl_LW sample up-regulated genes related to hair follicle morphogenesis and antigen presentation. The heterogeneity of fibroblast subclusters (Fig. 2D) might explain the reason why small wound generally heal with scarring devoid of HFs. In accordance with previous report(3), the major initial wave of dermal repair in small wound is mediated by the lower lineage fibroblast including LF (49.88%) and RF (21.93%), which were related to collagen deposition in hypodermis and dermis (fig. S2D). In contrast, there were more upper lineage PF (36.11%) in large wound. The PF consisted of 2 subclusters including PF1 ($Runx1^{+}Inhba^{+}$)(4) and PF2 ($Notch1^{+}Prdm1^{+}$)(11), both of which were believed to have the capacity to support HF initiation (fig. S2D). Scoring spots in each section with fibroblast-signature genes from scRNA-seq (fig.S2) showed that the PF (HF-related) exhibit strong spatial preferences within the large wound center (Fig. 2E). To explore how distinct immune cell types may contribute to the healing procedure, the heterogeneity of immune cell subclusters were evaluated next. There were more monocyte (Mono), anti-inflammatory macrophages (AIM) and pro-inflammatory macrophages (PIM) from Ctrl_LW group (Fig. 2F). As shown in Fig. 2G, Mono, PIM, and AIM diffusely distributed in small wounds, while Mono (related to antigen presentation) and PIM (related to pro-inflammatory pathways) showed the preferentially aggregation in large wound center. Besides, the Ctrl_LW group showed the higher proportion of adaptive T cells (Fig. 2H). Almost all T cell subclusters were exclusively expressed in large wound center (Fig. 2I). In contrast, there seem lack observable T cell infiltration in small wound. To sum up, it was in large wound that we observed the preferential aggregation of PF (related to HF regeneration) as well as adaptive T cells, Mono and PIM, which laid the foundation the potential cellular communication among them.

Cellular communication landscape between immune cell and HF-related cutaneous cell

Next, to address potential interactions between defined cell subclusters (Fig. 3A, fig. S2~S4), Cell Chat(*17*) was applied to predict the cell-cell communication patterns at the level of ligand/receptor expression (Fig. 5B). By comparing the interaction strength (information flow),

we could identify signaling pathways decrease (turn-off) or increase (turn-on) in different biologic conditions. We selected up-regulated pathways and compared the overall signaling strength of ligand-receptors that exhibit different signaling patterns (Fig. 3C). Adaptive immune system related pathways including MHC-I, MHC-II and CD80 was exclusively enriched in large wound. The major signaling among immune cell and cutaneous cell in large wound was mediated by PF (related to HF regeneration). As shown in Fig. 3D, adaptive immune cells and hair follicle precursor cells were enriched for interacting ligand or receptor gene partners such as Il6/Il6st, Inhba/Acvr1b. Spatial plots showed the preferentially aggregation of Il6 and Inhba in large wound. The essential role of activin(*18, 19*) and Il6(*11*) pathway in HF regeneration has been reported. Our result suggested that immune cell especially T cells, Mono and PIM may modulate the states of PF, Hair follicle progenitor (HFP) and Hair follicle stem cell (HFSC) through signaling pathways such as IL-6 and activin.

Enhanced WIHN occurred in scaffold-implanted wound with the further activation of adaptive immune system

Synthetic graft transplantation is one of the efficient treatments for severe large area wound of skin especially when patient's donor site is not qualified(*2*). With the further understanding of tissue engineering, it is suggested that synthetic biomaterials imitating the native structure of native ECM structure can integrate and play potentially pro-regeneration role to wound healing(*13, 20*). Our previous report has illustrated the immuno-regulatory effect of ECM scaffold in small wound (diameter=0.6cm) healing(*15, 16*). We next repeated large full-thickness wound-healing model in C57BL/6 mice with/without implanted biomaterial to investigate if the further regenerative phenomenon observed in ECM scaffold treated wounds. Workflow for evaluating large wound healing was summarized in Fig. 4A. We placed ECM scaffolds below the full-thickness excisional wound (diameter,1.5 cm; Fig. 4B) in ECM_LW group, while the Ctrl_LW group received no materials. Wound coverage was faster in the ECM_LW group (Fig. 4, C and D), and the ECM_LW also had the smaller gap width (Fig. 4. E and G). IF staining for cytokeratin 5 (Krt5) and cytokeratin 10 (Krt10) showed the keratinocyte around the biomaterials (Fig. 4I) , and the ECM_LW group had the larger area of neo-epithelium (Fig. 4J). As showed in Fig. 4F, the ECM membrane implanted in large wound did not trigger an obvious fibrous capsule. The scaffold owned a rapid degradation rate in vivo. We could observe the degrading fragments on POD 14 and degrading particles on POD21, and there were not any visible remaining on POD28 (Fig. 4F). In addition, the outline of HF morphogenesis could be

recognized in ECM_LW group: with the first appearance in hair germ stage on POD7, they gradually grew into bulbous-peg structure overlaid the degrading scaffold fragments on POD21. On POD28, we found that ECM_LW group recapitulated normal skin architecture with equivalent number of mature appendages and "basket-wave" ECM collagen deposition (Fig. 4H). In summary, in mice large full-thickness wound model, the biomaterial led to the faster wound healing and enhanced regeneration of HF. The excellent biocompatibility and degradability of membrane also avoid the risk of immune rejection and secondary surgery in further clinical applications. To explore the underlying mechanism, we noticed the ECM_LW group showed increased enrichment of genes involved in the hair follicle development as well as T cell differentiation (Fig. 4K). IF & IHC staining, and flow cytometry confirmed the increased T cell infiltration around implanted biomaterials (Fig. 6J).

Integration of ST and scRNA-seq illustrated the cell heterogeneity around biomaterials

To explore the spatial characteristic of cell heterogeneity in scaffold-implanted wound, we also applied the ST and scRNA-seq to analyze spatial gene expression profile(Fig. 5A). The anatomical structure could also be identified in ST sections (Fig. 5B), and the ECM_LW showed the gene enrichment in hair follicle morphogenesis as well as adaptive immune response (Fig. 5C). Based on scRNA-seq analysis, the ECM_LW group showed the higher proportion of HF related fibroblast and keratinocyte (fig. S7~S9). Spatial feature plot showed the keratinocyte around implanted biomaterials (Fig. 5D). What's more, we observed that the distribution of upper lineage PF (related to HF regeneration) was enlarged in ECM_LW group. In contrast, lower lineage fibroblasts including RF and LF (related to collagen deposition) were significantly reduced (Fig.5 E) which indicated the different healing outcome. Although generally the HF formation procedure would not start until several days after wound closure in large wound without implantation (POD14~21) (*4*). In ST profiling of ECM_LW group on POD7, we could identify the initial structure of HF composed of Krt28^{+}HFP in neo-epidermis and Twis2^{+} Dermal condensate (Dc) aggregation beneath in dermis (Fig. 5F), which highlighted the early HF formation signature in ECM_LW group at the spatial gene expression level (Fig. 5G).

To explore the scaffold-induced immune microenvironment, we next integrated the marker genes of immune cells with ST profiling. Spatial plot of each cluster in ST sections were shown in Fig. 5H and 5I. We noticed the obvious aggregation of MAC surrounding the membrane. The enlarged distribution of the T cell around biom. Notably, we observed the accumulation of tissue resident ILC in epithelium as well as granulation tissue particularly in ECM_LW group. ILCs

near epithelium might potentiated the cellular communication with HFSC or HFP cells, and thus help HF formation. Based on the multimodal profiling, we still observed the overlapping distribution of T cell, PIM, and Mono with the HF precursor cells in ECM_LW group, which implied the potential cellular communication among them.

Prediction of critical signaling patterns between spatially colocalized cell populations of ECM_LW and Ctrl_LW

Next, we also applied Cell Chat to predict the cell-cell communication patterns between EMC_LW and Ctrl_LW (Fig. 6 A and B). The heatmap showed the overall signaling strength of ligand-receptors in Ctrl_LW and ECM_LW group (Fig. 6C).Adaptive immune system related pathways including MHC-II was activated in ECM_LW. In addition to IL6, the key signaling in embryonic HF development such as FGF(*21*), Notch(*22*), KIT (*17*) were up-regulated in ECM_LW group. Remarkablely, T cell subclusters (especially ILC) and HF precursor cell were enriched for interacting receptor /ligand gene partners including Areg-(Egfr+Erbb2), Epgn- Egfr (Fig.6 D and E). The critical functions of Egf pathway in embryogenic skin morphologies has been predicted(*17*), and the expression of epidermal growth factor receptor (Egfr) was believed to be essential for Treg cells to facilitate cutaneous wound healing(*23*). Based on our analysis, the T cells (especially ILC) might modulate the HF precursor cell growth through EGF and EGPN pathways, and thus facilitate the HF formation. In addition, as shown in Fig. 6E we observed that the immune cells (macrophage and T cell subclusters) and HF precursor cell were enriched for interacting receptor or ligand gene partners including Mdk-(Sdc1 or Itgb1), Ptn-(Itgb1or Sdc1). The role of pleiotrophin (PTN) and midkine (MK) pathways in mice epidermal stratification event occurred between E13.5 and E14.5 was stressed(*17*).Based on our prediction, HF precursor cells could reversely mediate the activation of immune cell through regional cellular communications such as Mk and Ptn pathways as well. To testify the role of adaptive immune systems in HF regeneration , we placed ECM scaffolds in the dorsal skin large wound in immunodeficient C57Bl/6 (B6.129-Rag2tm1) mice, which lacked mature T lymphocytes (Fig. 6 F and G). We noticed wound closure rate was delayed in Rag2−/− mice (Rag2−/−) (Fig. 6 H~J). Regeneration of HF was scarce in Rag2−/− mice (Fig. 6K). Compared to WT mice which recruited the Cd3+ T cell, we observed the Ly6g+ neutrophils in Rag2−/− mice instead.

Biomaterials facilitated the de novo HF regeneration despite of wound size

To detect if there still any difference in wound healing between small or large wound treated with biomaterial, we next repeated small (diameter=0.6cm) and large (diameter=1.5cm) full-

thickness wound implanted with biomaterials (fig.S11 A and B). Consistent with ECM_LW group, the aligned membrane implanted in small wound did not trigger an obvious FBR fibrous capsule either (fig. S11C). There was no significant difference in thickness of fibrous capsule around scaffold between small and large wound (fig. S11D). The scaffold still owned a rapid degradation rate in small wound. We could identify the degrading fragment on POD14, and there was not any visible remaining on POD28 (fig. S11C). Histological sections of the ECM_SW tissue also revealed clear signs of enhanced WIHN (fig. S11C): On POD14, neo-epithelium of small wounds displayed bulbs and under there were several epidermal cysts, while the dermis was thicker wrapping the degrading scaffold fragments. Subsequently, we observed mature HFs featured SG on POD28. Similarly, de novo hair follicle in ECM_SW group was zigzag without pigmentation (fig. S11E). The difference of average HF numbers between two groups was not statistically significant as well (fig. S11F). Based on bulk-seq profiling, heatmaps showed insignificant changes of gene expression related to HF regeneration, adaptive immune response, or innate immune response (Fig. S11G). IHC staining for Cd3 and Cd68 confirmed the resembling infiltration level of T cell and macrophage surrounding the scaffold or in granulation tissue (Fig. S12 H and I). We further explored the differences in immune cell composition using scRNA-seq (Fig. S12A). The total proportion of macrophage was equilibrium between two groups (Fig. S13A), and the integrated analysis of ST profiling showed the similar distributions of three subsets around the scaffold (Fig. S13A). Despite the slight difference in T cell subclusters composition, multimodal analysis confirmed the substantial distribution of all T cell subsets surrounding the scaffold in both groups (Fig. S13G). In summary, based on our evaluation, the biomaterial showed similar “pro-regenerative” effect on would healing despite of wound size. Besides, the resembling immune-regulatory effect on adaptive immune system indicating the significant role of local immune environment in HF regeneration.

Discussion:

Problems including delayed would closure, susceptibility to infection, and inability of regenerating appendages have become the main impediment for skin wound healing(*24*). Requirements for appropriate biocompatibility, degradability, and ability to accelerate epithelialization as well as promote nascent HF formation bring significant challenges to biomaterial design, particularly for large-scale full-thickness wound. WIHN is a rare model of mammalian organ regeneration in adult mice wherein large full-thickness wound (>1cm^2) induce few nascent HF regeneration limited in wound center(*4*). The initiation of HF morphogenesis

begins when the HFP(*25*) and HFSC(*9*) migrating with neo-epithelium and induced the aggregation of Dc (derived from PF) under them(*26*). The pro-regenerative influence of the immune system in coordinating the early stage of wound repairing has been stressed(*27*). However, the cellular interplay between specific immune subclusters and HF precursor cells remains unclear.Here, we firstly compared the transcriptomics profiles between total "scarring" (small wound, diameter = 0.6cm) and "half-regenerative" WIHN (large wound, diameter = 1.5cm) model. From our multimodal analysis of small (Ctrl_SW) and large wound (Ctrl_LW) samples, we observed the higher proportion of adaptive immune cell from Ctrl_LW group (Fig. 2 F and H), which resided in large wound center and margin co-localizing with HF precursor cells (Fig. 2 G and I). The active regional cell-cell communications among them indicated the "pro-regenerative" role of adaptive immune cells in promoting HF neogenesis and served as a promising therapeutic target for the application of immune-regulatory materials in skin wound regeneration (Fig. 3 D and E). Next, we employed the ECM scaffold for large area skin defect along with the investigation of its role in wound healing and immune microenvironment modulation. The scaffold showed the impact on accelerating wound closure and promoting the nascent HF formation (Fig. 4 E and H). It was shown that the biomaterial owned a regulatory impact on adaptive immune system. We identified that the substantial T cell infiltration in response to scaffold implantation was driven toward regenerative subpopulations, overlapping with the abundant PF (related to HF regenration) (Fig. 5 E, H and I). The local intercellular communications among the enlarged "pro-regenerative" immune niche with HF precursor cells supported the essential role of adaptive system in HF regeneration (Fig. 6 D and E). Lastly, we confirmed the pro-regenerative effect of scaffold in both small and large wound repairing (Fig. S11F). The scaffold showed the resembling effect on the recruitment of T cells (Fig. S12H and Fig. S12J). Meanwhile, the mild FBR around the scaffold decreased the risk of immune rejection, and the appropriate degrading rate could also avoid the extra expense of secondary surgery (Fig. S11 C and D). In conclusion,

regenerated when the wound was created during the telogen/catagen stage of hair cycle(*4, 30*). It deserved subsequent exploration about the activity of melanocytes in WIHN model.

References and Notes

1. C. Willyard, Unlocking the secrets of scar-free skin healing. *Nature* **563**, S86-s88 (2018).doi:10.1038/d41586-018-07430-w
2. D. Henn *et al.*, Xenogeneic skin transplantation promotes angiogenesis and tissue regeneration through activated Trem2(+) macrophages. *Science advances* **7**, eabi4528 (2021).doi:10.1126/sciadv.abi4528
3. M. Kurita *et al.*, In vivo reprogramming of wound-resident cells generates skin epithelial tissue. *Nature* **561**, 243-247 (2018).doi:10.1038/s41586-018-0477-4
4. M. Ito *et al.*, Wnt-dependent de novo hair follicle regeneration in adult mouse skin after wounding. *Nature* **447**, 316-320 (2007).doi:10.1038/nature05766
5. M. V. Plikus *et al.*, Regeneration of fat cells from myofibroblasts during wound healing. *Science (New York, N.Y.)* **355**, 748-752 (2017).doi:10.1126/science.aai8792
6. I. C. Boothby, J. N. Cohen, M. D. Rosenblum, Regulatory T cells in skin injury: At the crossroads of tolerance and tissue repair. *Science immunology* **5**, (2020).doi:10.1126/sciimmunol.aaz9631
7. B. A. Shook *et al.*, Myofibroblast proliferation and heterogeneity are supported by macrophages during skin repair. *Science (New York, N.Y.)* **362**, (2018).doi:10.1126/science.aar2971
8. D. Gay *et al.*, Phagocytosis of Wnt inhibitor SFRP4 by late wound macrophages drives chronic Wnt activity for fibrotic skin healing. *Science advances* **6**, eaay3704 (2020).doi:10.1126/sciadv.aay3704
9. X. Wang *et al.*, Macrophages induce AKT/β-catenin-dependent Lgr5(+) stem cell activation and hair follicle regeneration through TNF. *Nature communications* **8**, 14091 (2017).doi:10.1038/ncomms14091
10. D. Gay *et al.*, Fgf9 from dermal γδ T cells induces hair follicle neogenesis after wounding. *Nature medicine* **19**, 916-923 (2013).doi:10.1038/nm.3181
11. A. M. Nelson *et al.*, Interleukin-6 Null Mice Paradoxically Display Increased STAT3 Activity and Wound-Induced Hair Neogenesis. *The Journal of investigative dermatology* **136**, 1051-1053 (2016).doi:10.1016/j.jid.2015.12.043
12. P. Lee *et al.*, Stimulation of hair follicle stem cell proliferation through an IL-1 dependent activation of γδT-cells. *eLife* **6**, (2017).doi:10.7554/eLife.28875
13. B. Yi, Q. Xu, W. Liu, An overview of substrate stiffness guided cellular response and its applications in tissue regeneration. *Bioactive materials* **15**, 82-102 (2022).doi:https://doi.org/10.1016/j.bioactmat.2021.12.005
14. K. Sadtler *et al.*, Design, clinical translation and immunological response of biomaterials in regenerative medicine. *Nature Reviews Materials* **1**, 16040 (2016).doi:10.1038/natrevmats.2016.40
15. C. Hu *et al.*, Dissecting the microenvironment around biosynthetic scaffolds in murine skin wound healing. *Science advances* **7**, (2021).doi:10.1126/sciadv.abf0787
16. C. Wang *et al.*, The diameter factor of aligned membranes facilitates wound healing by promoting epithelialization in an immune way. *Bioactive materials* **11**, 206-217 (2022).doi:10.1016/j.bioactmat.2021.09.022
17. S. Jin *et al.*, Inference and analysis of cell-cell communication using CellChat. *Nature communications* **12**, 1088 (2021).doi:10.1038/s41467-021-21246-9
18. W. Wang *et al.*, Changes in regeneration-responsive enhancers shape regenerative capacities in vertebrates. *Science (New York, N.Y.)* **369**, (2020).doi:10.1126/science.aaz3090

19. C. Seo, M. Kwack, M. Kim, J. Kim, Y. Sung, Activin A-induced signalling controls hair follicle neogenesis. *Experimental dermatology* **26**, 108-115 (2017).doi:10.1111/exd.13234
20. M. Monavarian, S. Kader, S. Moeinzadeh, E. Jabbari, Regenerative Scar-Free Skin Wound Healing. *Tissue engineering. Part B, Reviews* **25**, 294-311 (2019).doi:10.1089/ten.TEB.2018.0350
21. K. Mok *et al.*, Dermal Condensate Niche Fate Specification Occurs Prior to Formation and Is Placode Progenitor Dependent. *Developmental cell* **48**, 32-48.e35 (2019).doi:10.1016/j.devcel.2018.11.034
22. N. Ali *et al.*, Regulatory T Cells in Skin Facilitate Epithelial Stem Cell Differentiation. *Cell* **169**, 1119-1129.e1111 (2017).doi:10.1016/j.cell.2017.05.002
23. A. Nosbaum *et al.*, Cutting Edge: Regulatory T Cells Facilitate Cutaneous Wound Healing. *Journal of immunology (Baltimore, Md. : 1950)* **196**, 2010-2014 (2016).doi:10.4049/jimmunol.1502139
24. S. Mascharak *et al.*, Preventing Engrailed-1 activation in fibroblasts yields wound regeneration without scarring. *Science (New York, N.Y.)* **372**, (2021).doi:10.1126/science.aba2374
25. M. W. Hughes *et al.*, Msx2 Supports Epidermal Competency during Wound-Induced Hair Follicle Neogenesis. *The Journal of investigative dermatology* **138**, 2041-2050 (2018).doi:10.1016/j.jid.2018.02.043
26. V. Thulabandu, D. Chen, R. P. Atit, Dermal fibroblast in cutaneous development and healing. *Wiley interdisciplinary reviews. Developmental biology* **7**, (2018).doi:10.1002/wdev.307
27. G. Wang *et al.*, Bacteria induce skin regeneration via IL-1β signaling. *Cell host & microbe* **29**, 777-791.e776 (2021).doi:10.1016/j.chom.2021.03.003
28. D. Griffin *et al.*, Activating an adaptive immune response from a hydrogel scaffold imparts regenerative wound healing. *Nature materials* **20**, 560-569 (2021).doi:10.1038/s41563-020-00844-w
29. S. Y. Chu *et al.*, Mechanical stretch induces hair regeneration through the alternative activation of macrophages. *Nature communications* **10**, 1524 (2019).doi:10.1038/s41467-019-09402-8
30. M. Yuriguchi, H. Aoki, N. Taguchi, T. Kunisada, Pigmentation of regenerated hairs after wounding. *J Dermatol Sci* **84**, 80-87 (2016).doi:10.1016/j.jdermsci.2016.07.004

Acknowledgments: We thank the Novogene company for RNA sequencing work, and the National Clinical Research Center for Oral Diseases & State Key Laboratory of Oral Diseases for animal experiment, and the Analytical & Testing Center of Sichuan University for the fabrication of biomaterials. We thank Jia-yu Gao and Sheng-an Rung for the help with analysis.

Funding: Sichuan Science and Technology Plan grant 2022YFS0041 (Y.L.Q.)

Interdisciplinary Innovation Project, West China Hospital of Stomatology Sichuan University grant RD-03- 202006 (Y.M.)

Research and Develop Program, West China Hospital of Stomatology Sichuan University grant LCYJ2019-19 (Y.M.)

Author contributions:

Conceptualization: YY, CYC

Methodology: CYC, LL, CH, CBW

Investigation: XHL

Visualization: YY

Writing – original draft: YY

Writing – review & editing: CCY

Funding acquisition & Project administration & Supervision: YM, YLQ

Competing interests: Authors declare that they have no competing interests.

Data and materials availability: All data to support the conclusions in this manuscript can be found in the figures and the supplementary materials. Any other data can be requested from the corresponding authors.

Supplementary Materials

Materials and Methods

Supplementary Text

Figs. S1 to S12

References (*39–##*)

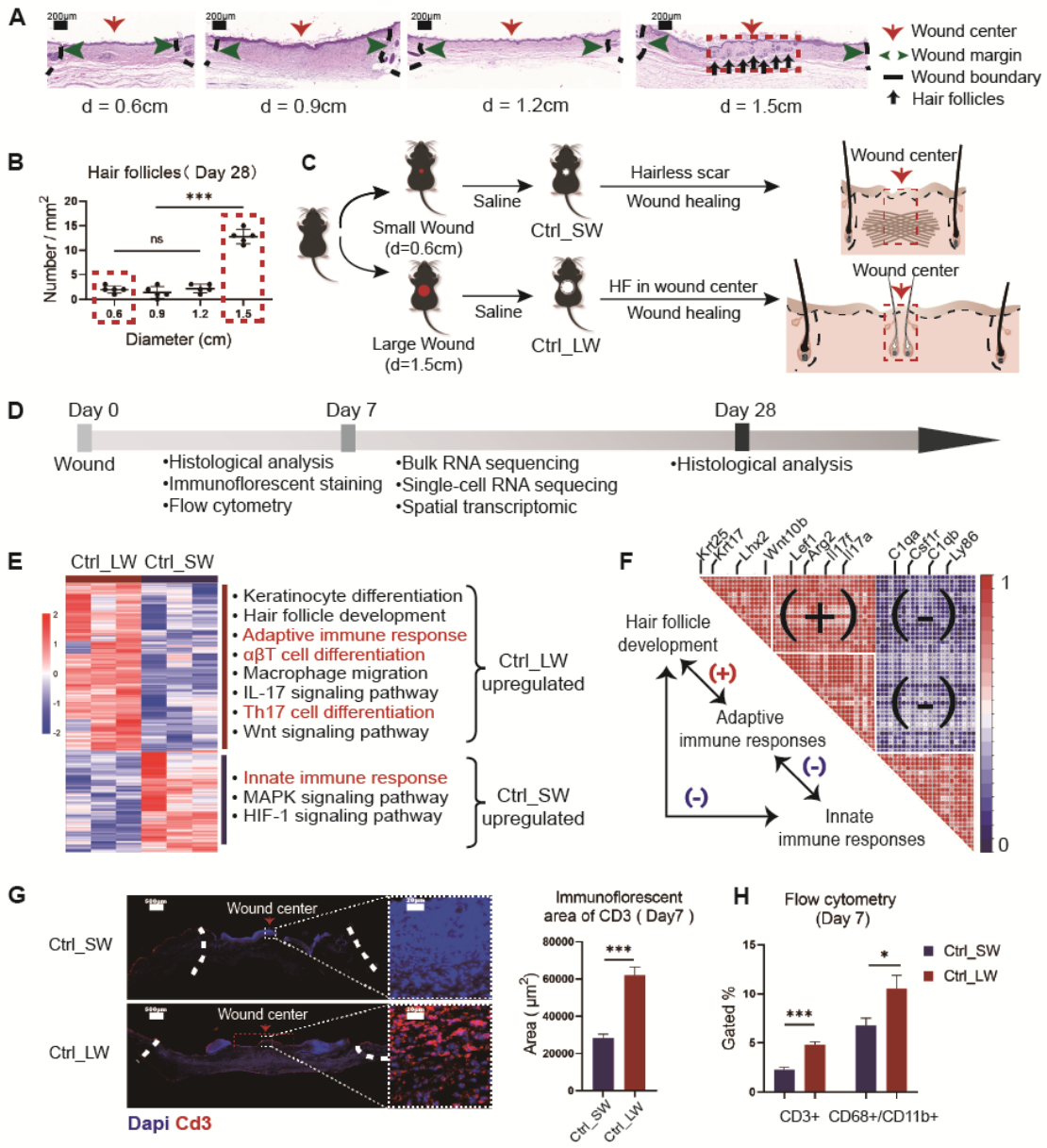

Fig. 1. Evaluation of the healing of small and large full-thickness wound. (A) Haematoxylin and eosin (H&E) staining evaluating skin wound healing outcomes of different wound size. (B) Histologic quantification of de novo hair follicles. (C) Surgical process for the mice full-thickness excisional splinted of small (Ctrl_SW) and large (Ctrl_LW) wound and different healing outcomes. (D) Workflow for evaluating mice skin wound healing of different wound size. (E) Heatmap showing hierarchical clustering of differentially expressed genes (p value<0.05 & |log2FC|> 1) , and gene set enrichment analysis showing the up-regulated GO terms and KEGG pathways between two groups. (F) Pearson correlation analysis shows relation

between the gene expression of hair follicle development related genes, adaptive immune responses related genes and innate immune responses related genes (positive, red; negative, blue). (G) IF staining of Cd3 (red) in histologic sections and corresponding quantification. (H) In vivo flow cytometry strategy using Cd3 to identify T cells; monocyte, and macrophages co-expressing the surface markers CD68 and CD11b, and the corresponding quantification.

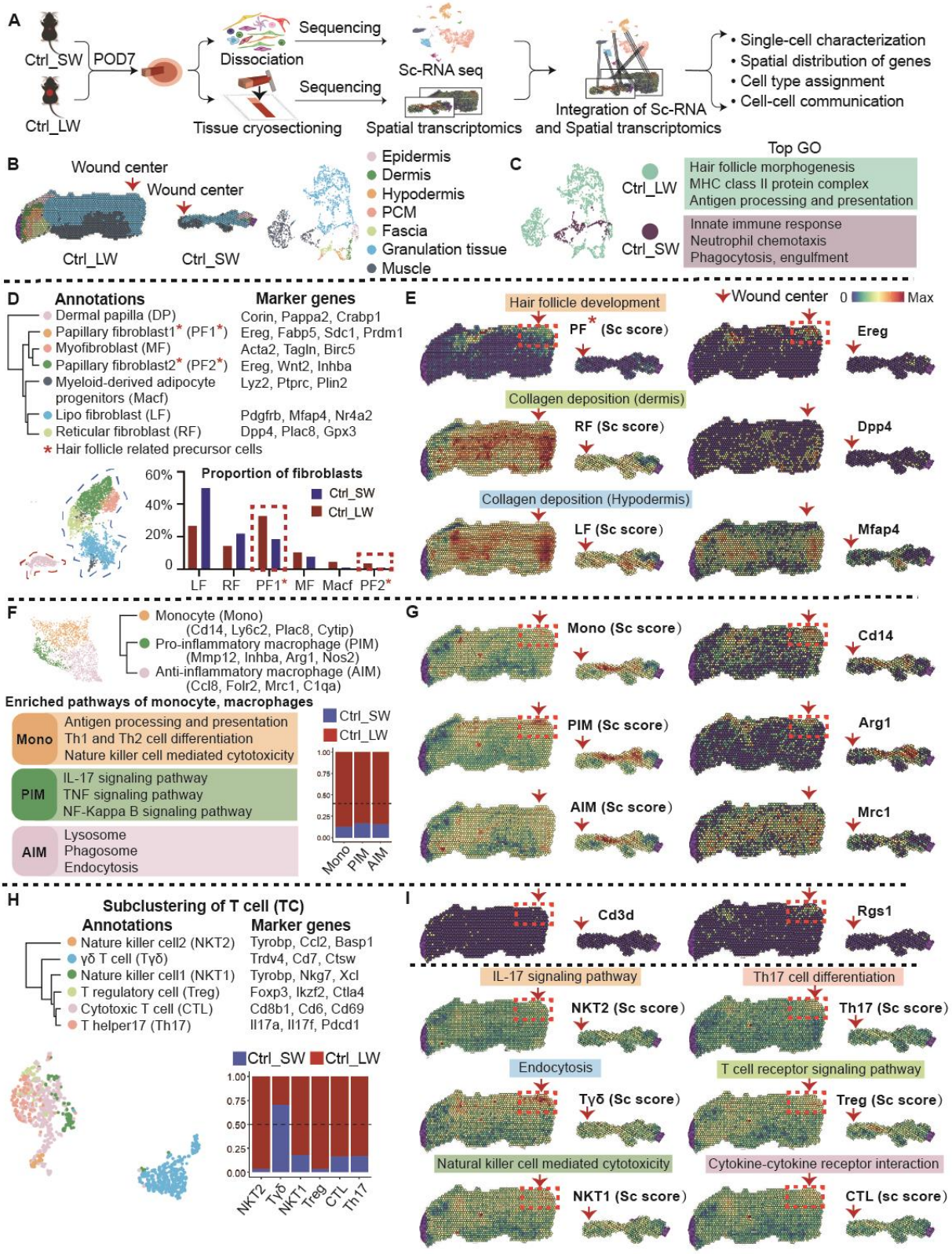

Fig. 2. Spatial transcriptomics applied to Ctrl_SW and Ctrl_LW. (A) Schematic for generating sc-RNA seq and spatial transcriptomics data from splinted excisional wounds. (B)

Spatial plots and UMAP plot showing that the anatomical regions could be distinguished by their transcriptional programs. (C) Gene enrichment analysis between Ctrl_SW and Ctrl_LW. (D) Subclustering of fibroblast in sc-RNA seq dataset. (E) Spatial feature plots showed defined fibroblast subclusters distribution in tissue sections. (F) Subclustering of monocyte, macrophages (MAC) in sc-RNA seq dataset (G) Spatial feature plots showed defined MAC subclusters distribution in tissue sections. (H) Subclustering of T cells (TC) in Sc-RNA seq dataset. (I) Spatial feature plots showed expression of Cd3d and Rgs1 (marker genes of TC) and defined TC subclusters distribution in tissue sections.

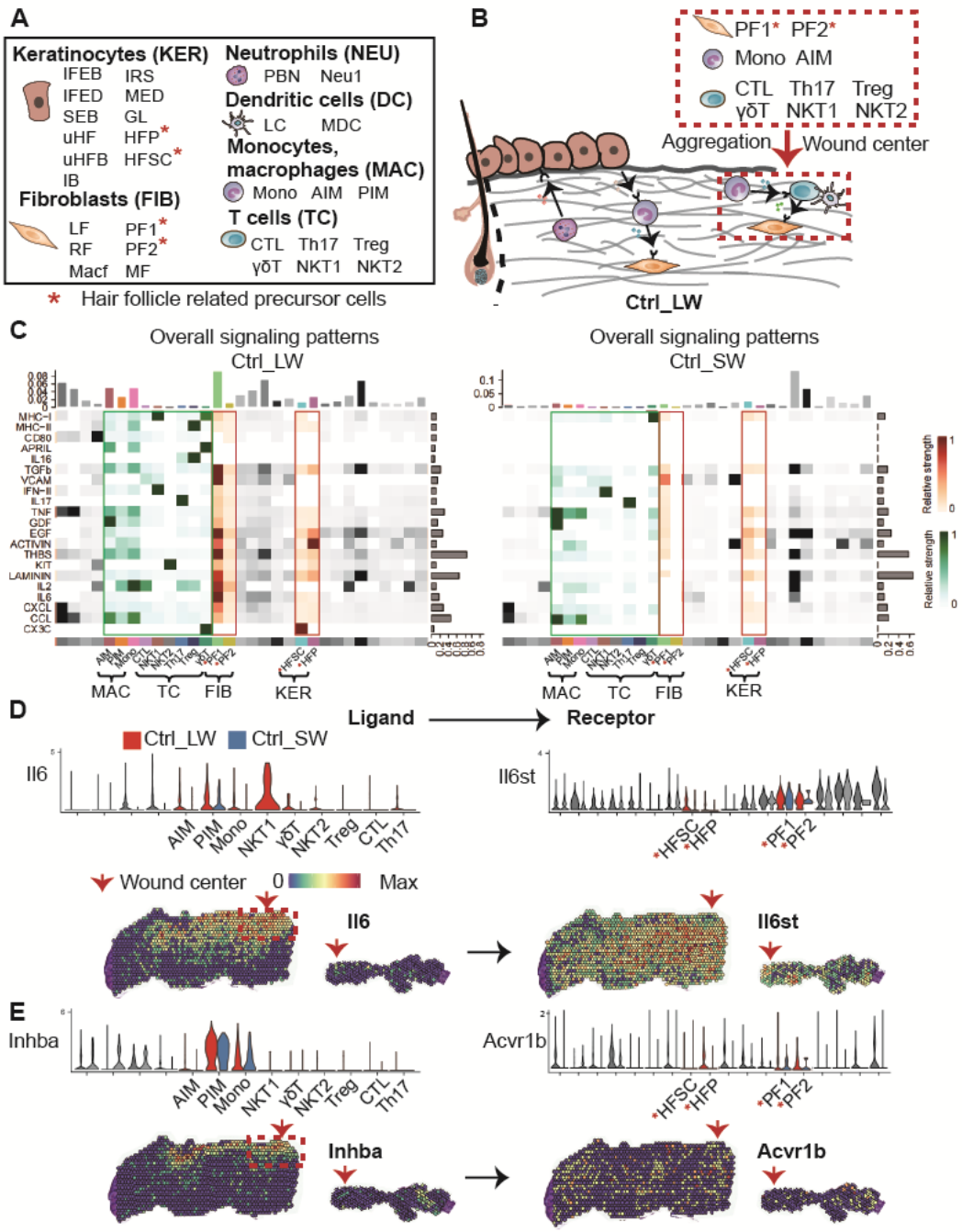

Fig. 3. Cellular communication landscape between immune cells and cutaneous cells in Ctrl_SW and Ctrl_LW. (A) Defined subclusters in sc-RNA seq dataset (related to Figure S2~S4) (B) Schematic of preferential aggregation of adaptive immune cells and papillary fibroblast in large wound center and combined ligand-receptor analysis between them. (C) Comparison of cell-cell communication patterns between Ctrl_SW and Ctrl_LW using CellChat.

(D&E) Violin plot (sc RNA-seq) and spatial feature plots (ST) showed selected ligands expressed by immune cell subpopulations and cognate receptor expression by HF precursor cells.

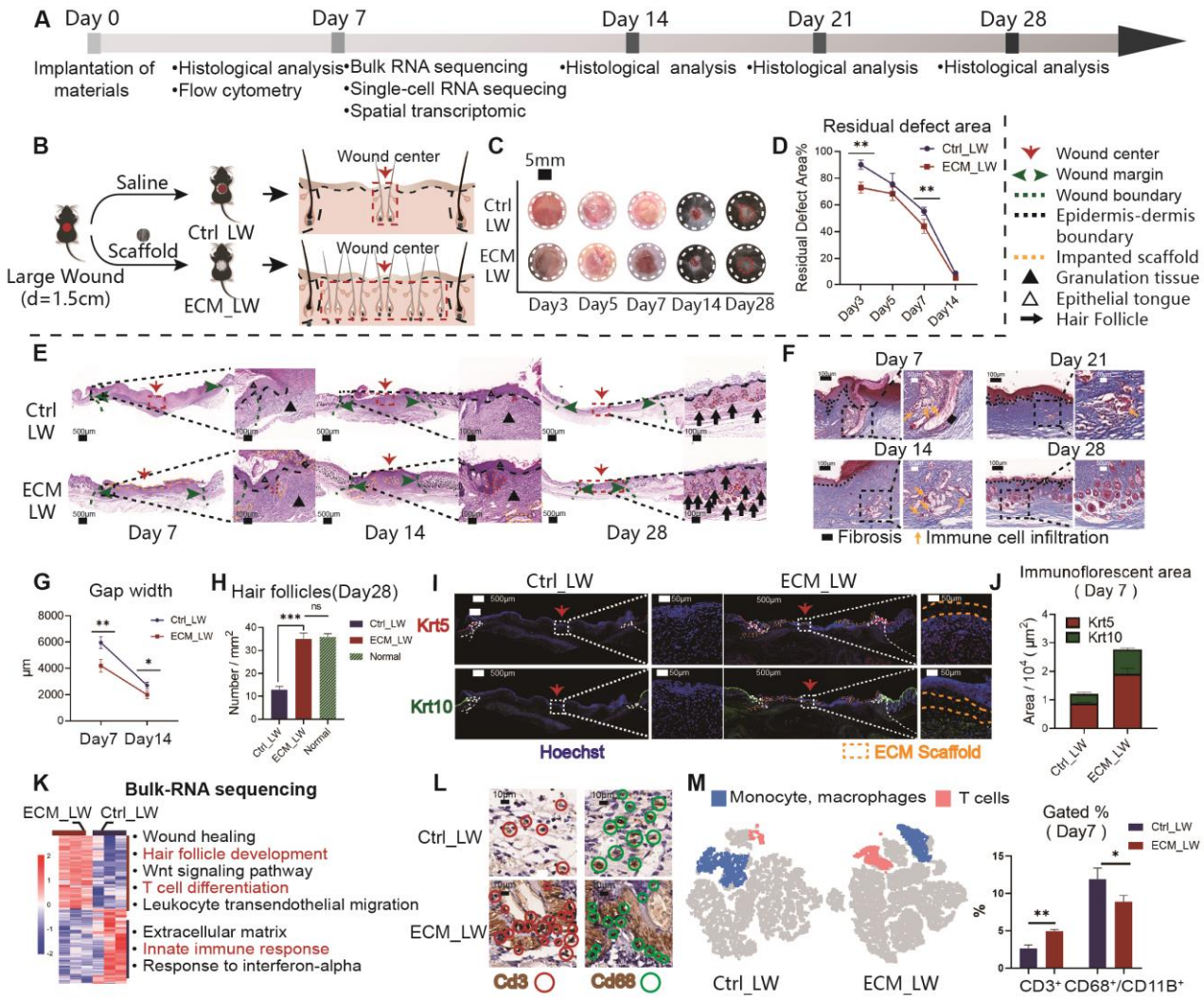

Fig. 4. Evaluation of the healing of large full-thickness wounds with/without implanted ECM scaffolds. (A) Workflow for evaluating large-scale wound healing. (B) Surgical processes for skin excisional wound model. (C) Residual wound area at 3, 5, 7, 14 and 28 days, and (D) corresponding analysis. (E) H&E analysis of two groups. (F) Evaluation of FBR around the biomaterials. Masson's trichrome staining for ECM_LW group on POD 7, 14, 21 and 28. (G) Semiquantitative evaluation of gap width. (H) Histologic quantification of de novo HFs on POD28. (I) IF staining using Krt5 (red) and Krt10 (green) and (J) semiquantitative evaluation of the fluorescent area. (K) Heatmap showing hierarchical clustering of differentially expressed genes (p value<0.05 & |log2FC|> 1) and gene set enrichment analysis. (L) IHC staining of Cd3 and Cd68. (H) In vivo flow cytometry strategy using Cd3 to identify T cells; monocyte, and macrophages co-expressing the surface markers CD68 and CD11b, and the corresponding quantification.

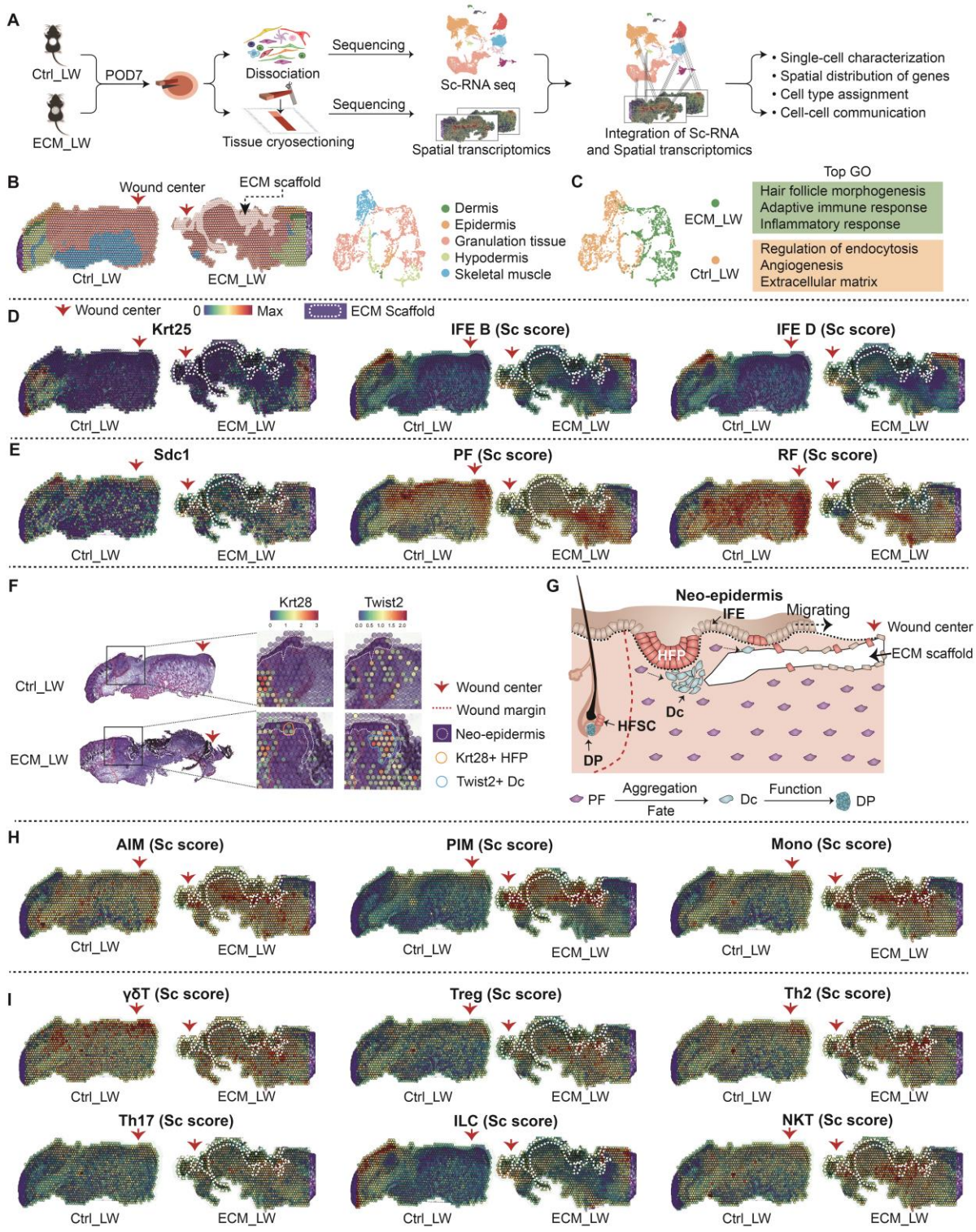

Fig. 5. Spatial transcriptomics applied to ECM_LW and Ctrl_LW. (A) Schematic for generating scRNA-seq and spatial transcriptomics data from splinted excisional wounds. (B) The unsupervised clustering indicated the anatomical structure of sample. (C) Gene enrichment

analysis between ECM_LW and Ctrl_LW. (D) SpatialFeaturePlot showed the expression of Krt25 (marker gene for keratinocytes from anagen HFs) and defined keratinocyte subclusters (related to Fig.S9) in tissue sections. (E) SpatialFeaturePlot showed the expression of Sdc1 (marker gene for papillary fibroblast) and defined fibroblast subclusters (related to Fig.S8) in tissue sections. (F) Spatial feature plot highlighted the expression of Krt28+ Hair follicle progenitor (HFP) and Twist2+ Dermal condensate (Dc) in migrating neo-epidermis. (G) Illustration showed the epithelialization along with de novo HF formation in ECM_LW group. (H) Defined monocyte, macrophage (MAC) subclusters (related to Fig.S8) in tissue sections. (I) Defined T cell subclusters (related to Fig.S9) in tissue sections.

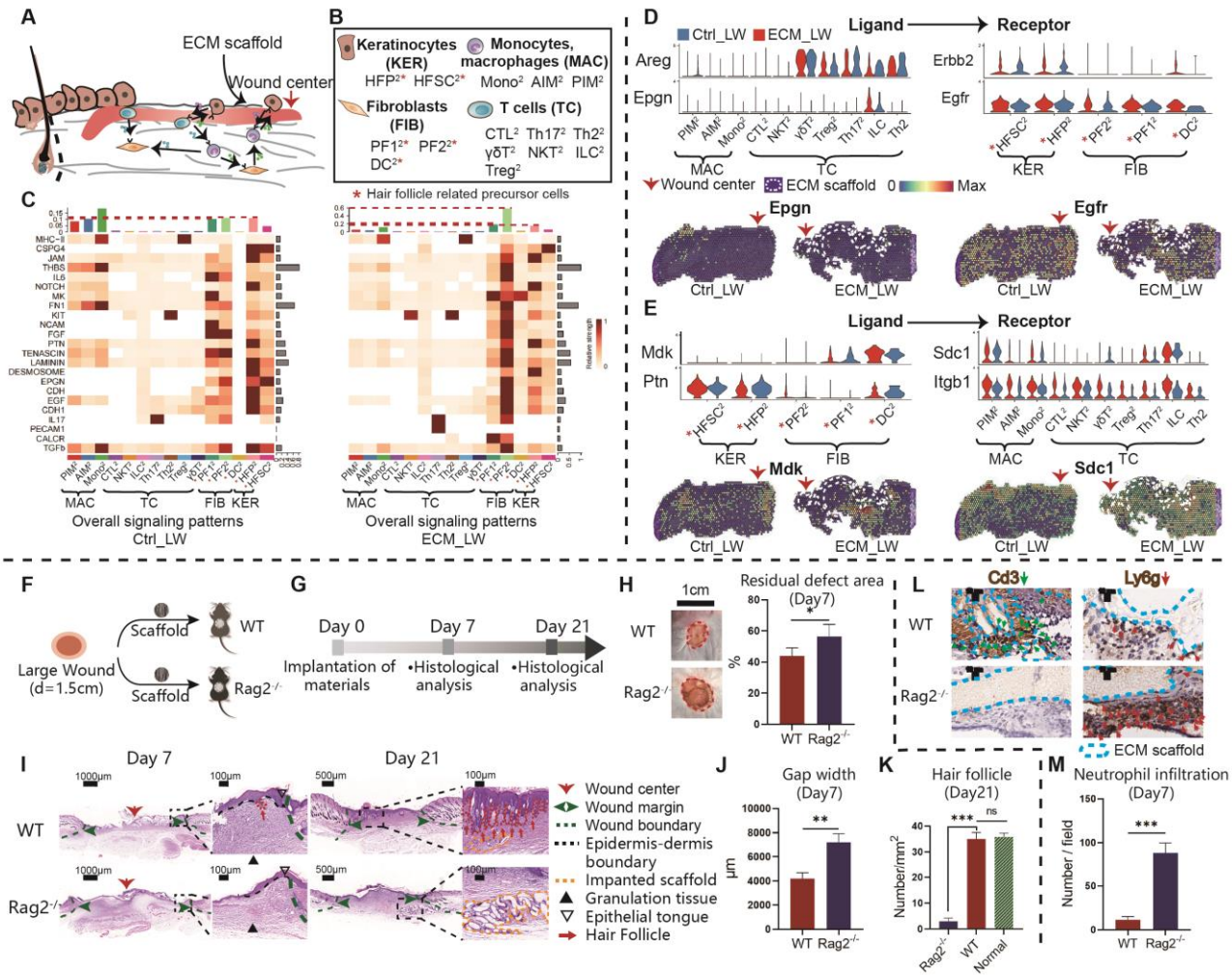

Fig. 6. Cellular communication landscape between immune cells and cutaneous cells in ECM_LW and Ctrl_LW group. (A) Schematic of combined ligand-receptor analysis between cutaneous cells and adaptive immune cells . (B) Defined subclusters in corresponding scRNA-seq dataset. (C) Comparison of overall cell-cell communication patterns between Ctrl_LW and ECM_LW using CellChat. (D and E) Violin plot (scRNA-seq) and spatial feature plots (ST) showed select ligands and cognate receptor expression. (F) Surgical process and (G) workflow for evaluating large area wound healing mediated by ECM scaffold in Rag2$^{-/-}$ and WT mice. (H) Residual defect area at 7 days after wound. (I) Histological analysis of wound healing in WT and Rag2$^{-/-}$ mice. (J) Semiquantitative evaluation of gap width. (K) Histologic quantification of de novo HFs. (L) IHC staining of Cd3 and Ly6g. (M) Quantification of Ly6g+ neutrophil infiltration.

Science

AAAS

Supplementary Materials for

Spatial anchor of adaptive immune cell around biomaterials mediated large scale wound regeneration

Yang Yang, Chen-yu Chu, Li Liu, Chen-bing Wang, Chen Hu, Xin-hui Li, Yi-li Qu*, Yi Man*

Correspondence to: manyi780203@126.com (Y.M.); qqyili@126.com (Y.L.Q.)

This PDF file includes:

Materials and Methods

Supplementary Text

Figs. S1 to S12

References (39–##)

Materials and Methods

Fabrication of ECM scaffolds

The preparation of ECM scaffolds was similar to our previous report(*1*).To fabricate the electrospinning scaffold with approximate 300nm diameter aligned fibers, 20% w/v PLGA (LA/GA = 75:25, molecular weight = 105 kDa, Jinan Daigang Biomaterial Co. Ltd.) and 2% w/v FC (Sangon Biotech Co. Ltd.) were dissolved in HFIP (Aladdin Co., Ltd.) with stirring until complete dissolution. The solution was fed at 0.018mm/min, and a voltage of -2/5kv and 11 cm distance between the needle (21G) and the rotating cylinder (2800 rpm) was applied. After been dried in a vacuum oven for a week, The morphology of PLGA/FC nanofibrous scaffold was observed by the scanning electron microscopy (SEM; JSM-7500F, JEOL, Japan). The scaffolds were cut into circular shape (0.8cm or 1.8cm in diameter) and sterilized using γ-irradiation before the animal implantation experiments.

Excisional wound model and implantation procedures

All procedures involving animals were approved by the Institution Review Board of West China Hospital of Stomatology (No. WCHSIRB-D-2017-033-R1). C57BL/6J mice (Dossy Experimental Animals Co., Ltd.) and immunodeficient C57Bl/6 (B6.129-Rag2tm1) mice (Shanghai Model Organisms Center Inc., Shanghai, China), at the age of 6 week (~20 g) were used in this research. The circular (diameter =0.6, 0.9, 1.2, 1.5cm) full-thickness wound were created in the mice dorsal skin. The mice in further study were divided into four groups: small wounds (diameter = 0.6cm) transplanted with saline (Ctrl_SW) or biosynthetic ECM scaffolds below the wound (ECM_SW), and large wound (diameter = 1.5cm) transplanted with saline (Ctrl_LW) or biosynthetic ECM scaffolds below the wound (ECM_LW). Subsequently, the wounds were covered with sterile Tegaderm film (3M) and respectively fixed on the small (inner diameter 8 mm and outer diameter 12 mm, for small wound) or large (inner diameter 18 mm and outer diameter 22 mm, for large wound) silicone ring with uniform suture. Mice were euthanatized at 1, 2, and 4 weeks after the surgery, and the small (diameter 10 mm, for small wound) or large (diameter 25 mm, for large wound) round full-thickness sample was harvested.

Bulk RNA sequencing

Three replicates of mice skin wounds in each group were collected for the of Bulk RNA sequencing procedure. Total amounts and integrity of RNA were assessed using the RNA Nano 6000 Assay Kit of the Bioanalyzer 2100 system (Agilent Technologies, CA, USA). mRNA was purified from total RNA by using poly-T oligo-attached magnetic beads. The library fragments were purified with AMPure XP system (Beckman Coulter, Beverly, USA). The PCR amplification product was purified by AMPure XP beads. After the library is qualified by qRT-PCR, the different libraries are pooling and being sequenced by the Illumina NovaSeq 6000. FeatureCounts (v1.5.0-p3) was used to count the reads numbers mapped to each gene. And then FPKM of each gene was calculated based on the length of the gene and reads count mapped to this gene. Differential expression analysis of two groups (three biological replicates per group) was performed using the DESeq2 R package (1.20.0), p−value <0.05 and $|\log_2(\text{foldchange})| > 1$ was set as the threshold for significantly differential expression. GO terms and KEGG pathways with corrected P-value less than 0.05 were considered significantly enriched by differential expressed genes.

Single cell RNA sequencing

Specimen harvest procedure for scRNA-seq was like our previous report(*2*),3~4 fresh samples were collected per group. In brief, the wound tissues were firstly digested by the Epidermis Dissociation Kit (Epidermis Dissociation Kit, mouse; Miltenyi Biotec) for enzymatic epidermal-dermal separation. The epidermis part was dissociated by a gentleMACS Dissociator (Miltenyi), then filtered (70-mm cell strainer, Corning, Durham), centrifuged (300g, 10 min, 4°C), and resuspended with phosphate-buffered saline (PBS) containing 0.5% bovine serum albumin (BSA). The dermis part was cut into 1 mm width pieces and mixed with mixed enzyme solution containing type I collagenase (Gibco, Grand Island) and trypsin (Gibco, Canada), then dissociated by gentleMACS Dissociator (Miltenyi), and digested for 2.5 hours in a hybridization oven (Peqlab PerfectBlot). After being dissociated, filtered, centrifuged, and resuspended in red blood cell lysis buffer (Solarbio), the dermis cells were mixed with epidermis part. Then the dead cells and debris were removed by Dead Cell Removal MicroBeads (Miltenyi). Lastly, these suspensions were then carried out for Single-Cell RNA-seq (10x Genomics Chromium Single Cell Kit). Sequencing (10x Genomics Chromium Single Cell 3′ v3) was performed using an Illumina 1.9 mode. Then, reads were aligned, and expression matrices were generated for downstream analysis (Cell Ranger pipeline software). Filtering, normalization, scaling and canonical correlation analysis were performed (Seurat 4.1.2.) for integrated datasets. CellChat was used to predict receptor-ligand probability among cell subpopulations.

Spatial Transcriptomics

Fresh samples were rapidly harvested and frozen in OCT. Wound tissues were cryosectioned at -20 degrees onto gene expression slides. Tissue sections on the Capture Areas of the Visium Spatial Gene Expression are fixed using methanol, H&E staining images will be used downstream to map the gene expression patterns. Using the Visium Tissue Optimization Slide & Reagent kit, permeabilization time was optimized. Second Strand Mix is added to the tissue sections to initiate second strand synthesis. After transfer of cDNA from the slide, spatially barcoded, full-length cDNA is amplified via PCR to generate sufficient mass for library construction. The final libraries contain the P5 and P7 primers used in Illumina amplification. A Visium Spatial Gene Expression library comprises standard Illumina paired-end constructs which begin and end with P5 and P7.Raw FASTQ files and histology images were processed (SpaceRanger software) for genome alignment. Raw output files for each group were read into R studio (Seurat 4.1.2). Normalization across spots was performed with the SCTransform function. The spatial cluster gene signature overlap correlation matrix was generated by first taking all genes differentially expressed (avg_log2FC > 1 and adjusted p value < 0.05) across all ST clusters. Pearson correlation was calculated across this matrix and hierarchical clustering of ST clusters was performed with the heatmap function with the ggplots package. Signature scoring derived from scRNA-seq and ST signatures was performed with the AddModuleScore function.

Histopathology, Immunohistochemistry, and immunofluorescence microscopy

The samples were fixed with 4% paraformaldehyde at least 48 hours before ethanol and xylene dehydration. H&E staining and Masson's trichrome staining were performed for the observation of re-epithelialization and collagen fiber deposition. Immunofluorescence staining for cytokeratin 5 (ab52635, Abcam, 1:200) and cytokeratin 10 (ab76318, Abcam, 1:150) and was performed for to assess keratinization. For the evaluation the infiltration of immune cells, immunohistochemistry staining for Cd3 (14-0032-82, Thermo Fisher Scientific, 1:100), Cd68 (ab283654, Abcam, 1:100), Ly6g (ab238132, Abcam, 1:2000) and immunofluorescent staining for Cd3 (14-0032-82, Thermo Fisher Scientific, 1:100), Cd68 (ab201844, Abcam, 1:250) were performed.

Flow cytometry analysis

The surface markers of T cells (CD3), monocyte, and macrophages (CD11b, CD68) were examined using flow cytometry to quantification the infiltration of immune cells. The digested cell solutions were coincubated with antibodies against CD68 (Allophycocyanin, ab221251, Abcam), CD3 (fluorescein isothiocyanate, catalog no. 100203, BioLegend), and CD11b (PerCP/Cy5.5, catalog no. ab210299, Abcam) at 1:400 dilution for 30~60 min at 4°C in the dark (100 μl per antibody per sample). Before the staining of CD3, cells were preincubated with purified anti-CD16/CD32 antibody (catalog no. 101301, BioLegend) (1.0 μg per 10^6 cells in 100 μl volume) for 5 to 10 min to block Fc receptors. Flow cytometry analysis was performed using Attune Nxt flow cytometer (Thermo Fisher Scientific) and FlowJo 10.8.1. The experiments were performed three times independently (n = 3).

Statistics and reproducibility

At least three independent replicates were conducted to obtain repeatable data, and the data was dealt with Case Viewer software, Image J software, and Prism 8.0 software. Statistical analyses were performed by Student's t-test or one-way analysis of variance (ANOVA) with Tukey post-hoc test. The numerical data are presented as mean ± standard deviation. A value of $p < 0.05$ was considered statistically significant (*$p < 0.05$, **$p < 0.01$, ***$p < 0.001$), and ns means no statistically significant difference.

Supplementary Text

Cell type annotation of scRNA-seq data

Ctrl_LW VS Ctrl_SW

Firstly, we undertook scRNA-seq to compare the transcriptional profiling between Ctrl_SW and Ctrl_LW group at single-cell resolution (Fig. S1A). After quality control, 18,621 cell were included in the final dataset (11,217 from the Ctrl_LW group and 7,404 from the Ctrl_SW group). We firstly categorized the cells into 10 main clusters based on gene expression profiles using Seurat, and the proportion of cells from two groups were shown in Fig. S1B. Top (based on average |log2FC| value) marker genes for each cell cluster were shown in the Fig. S1C.

Subclustering of fibroblast

Firstly, we extracted cells defined as fibroblast and performed subcluster analysis (Fig. S2A) based on marker genes profiles published before(*2-9*) (Fig. S2B).Since dermal papilla (DP) cells ($Papp2^+Corin^+$) belonged to the existing HF in normal skin adjacent to the wound, which was not the focus of this part. We next conducted in-depth analysis of wound fibroblasts and defined them as following categories: upper layer papillary fibroblast (PF) ($Crabp1^+Fabp5^+$), lower layer fibroblast including reticular fibroblasts (RF) ($Dpp4^+Mgp^+Gpx3^+Plac8^+$) & hypodermis lipo-fibroblast (LF) ($Mfap4^+$ $Cd34^+$), as well as wound-activated myofibroblast ($Acta2^+Tagln^+Mki67^+$) and myeloid-derived adipocyte progenitors (Macf) ($Pdgfra^+$ $Lyz2^+$ $Ptprc^+$ $Plin2^+$).

Subclustering of keratinocyte

Next, we extracted cells assigned as keratinocyte and performed subcluster analysis. Known markers(*2, 8, 10-12*) were used to define keratinocyte subclusters identity (Fig. S2, E and G). Hair follicle stem cell (HFSC) ($Lgr5^+Lrig1^+$)(*12*) and HFP (hair follicle progenitor) ($Msx2^+Krt28^+Mki67^+$)(*11*) were believed to be the dominant epithelial contributor to the de novo HF. The proportion of HFP was higher in Ctrl_LW (12.97%) than Ctrl_SW (3.14%). Collectively, the higher proportion of HF precursor cells including PF (mesenchymal origin), HFSC and

HFP (epithelial origin) may account for the initiation of WIHN specially in large wound. Besides, since the HF cycles through phases of growth (anagen), regression (catagen), and rest (telogen)(*8*). Keratinocytes could be robustly assigned to two cell types: permanent part of the epidermis (interfollicular epidermis, sebaceous gland, and non-cycling portion of the HF) and keratinocytes from the cycling part of the anagen HF. The anagen HF cells in this dataset were composed of (Ube2c^{+}Ccnb1^{+}) germinative layer (GL) cells, (Mt4^{+} Rnaset2b^{+}Krt35^{+}) medulla (MED) and cortex cells, and (Krt25^{+}Krt27^{+}) inner root sheath (IRS) layers cells. Since the C57/B6 mice were in their second telogen (postnatal days P46–70) on POD7.The higher proportion of anagen HF cells in Ctrl_LW suggested a stronger HF telogen–anagen transition (TAT) around the large wound as well.

Subclustering of monocyte and macrophages

Macrophages are highly plastic immune cells upon different environment stimulators and contribute to most phases of tissue repair(*13*).They phagocytose pathogens or debris instantly in response to wounding. Then, they activate the adaptive immune system through specific antigen presentation, which is believed to bridge the innate and adaptive immune system(*14*).To explore the heterogeneity of macrophages, we extracted the monocyte and macrophages (MAC) and subjected them to further subcluster analysis. Canonical classification systems of macrophages including “classically activated” M1 macrophages and “alternatively activated” M2 macrophages were shown insufficiently to identify the phenotypes in this condition (Fig. 3B).Based on known markers(*2*), three subsets including Ccl8^{+} Folr2^{+}C1qa^{+}Mrc1^{+} anti-inflammatory macrophages (AIM), Mmp12^{+}Arg1^{+}Inhba^{+}Nos2^{+} pro-inflammatory macrophages (PIM) and Ly6c2^{+}Plac8^{+}Cytip^{+}H2-Eb1^{+} monocyte (Mono) were determined (Fig. 3, A and C). The pseudo-temporal trajectory of the three subsets revealed that monocytes developed into PIM firstly and then polarized into AIM (Fig. 3E). KEGG enrichment analysis revealed that Mono might play role in antigen presentation and T cell differentiation, and Mono in Ctrl_LW group specifically related to nature killer cell mediated cytotoxicity; PIM was related to pro-inflammatory pathways, among which IL-17 pathway was up-regulated in Ctrl_LW group; AIM was correlated to lysosome, phagosome, and endocytosis which belonged to innate immune response (Fig. 3D).The higher proportion of all three macrophage subsets as well as neutrophil and dendritic cell in Ctrl_LW (Fig. S2) suggested there was a more complex environment both in innate immune response as well as the activation of adaptive system in large wound.

Subclustering of T cells

Recently, the role of adaptive immune cells on the formation of the pro-regenerative immune microenvironment has been stressed out(*15*). Although the role of γδ T cells in facilitating WIHN (*16*, *17*) has been demonstrated, the relationship of adaptive immune cells with HF regeneration is largely unknown till now. The proportion of T cell was higher in Ctrl_LW group (Fig. S2B) in accordance with the result of bulk-seq and histological results. Based on published marker(*2*, *18*), T cells were clustered into seven subsets (Fig. 3, F and G) including Cd8b1^{+} cytotoxic T cell (CTL), Tyrobp^{+}Nkg7^{+}Xcl^{+} nature killer T cell1 (NKT1), Tyrobp^{+}Ccl2^{+} nature killer T cell2 (NKT2), Il17f^{+} T helper17 (Th17), Foxp3^{+} T regulatory cell (Treg), Trdv4^{+}Cd7^{+}Ctsw^{+} γδT cell1 (Tγδ1) and Cd7^{+}Ctsw^{+}Gnb21l^{+} γδT cell2 (Tγδ2). As shown in Fig. 3F, γδT cell was the only predominant subtype of T cell in Ctrl_SW (70.82%), which was related to endocytosis belonging to innate immune system (Fig 3H). In contrast, there were more abundant subtypes of adaptive αβT cells in Ctrl_LW group, which were related to Th17 and Th1/Th2 cell differentiation (Fig. 3H). Besides, the proportion of Ccl2^{high} NKT2 cell was also higher in Ctrl_LW, which was related to the recruitment

of inflammatory macrophage(*19*). What's more, there were more Tregs in large wound which were believed to paly role in suppressing excessive collagen deposition and driving HFSC differentiation &migration(*20*). To sum up, the diverse subtypes of T cell from Ctrl_LW group suggested a more active adaptive immune micro-environment in skin large wound.

ECM_LW vs Ctrl_LW

To explore how ECM scaffold regulated the microenvironment in large wound, we isolated cells from the ECM_LW and Ctrl_LW samples and applied them to the 10x scRNA-seq platform (Fig. S8A). After cell filtering, 31,740 single-cell transcriptomes were included in the final dataset (20,312 for the ECM_LW group and 11,428 for the Ctrl_LW group). Unsupervised clustering using Seurat categorized the cells into 10 main classes of cells. The composition of each cell cluster was listed so that the proportion of cells from two groups could be identified across all cell clusters (Fig. S8B). Marker genes for each cell cluster were shown in the heatmap in Fig. S8C. Genes related to T cells (Il7r, Areg and Tubb5) were substantially higher expressed by the ECM_LW (Fig. S8D).

Subclustering of fibroblast

Firstly, As shown in Fig. 7A, we defined most fibroblast subclusters based on defined markers in Fig. 2B. Remarkably, we identified the Smad3^{+}Lef1^{+}Krt17^{+} dermal condensate (Dc) cell(*21*) specially in this dataset. Derived from PF, The Dc was believed to be the origin of DP reside at the base of the adult HF (*21, 22*).Since approximate 90% of Dc were from ECM_LW group, as well as significantly higher proportion of PF1^{2} and PF2^{2} from ECM_LW (Fig. 7B), which might provide enough mesenchymal component for the subsequent HF formation in ECM_implanted group. In embryologic HF morphology, Dc is believed to be the signaling niches for epithelial HFP to form epithelial placode (Pc)(*21*), and thus promote HF growth.

Subclustering of keratinocyte

Based on known marker in Fig. 2F, we also find the higher proportion of HFP^{2} and HFSC^{2} in ECM_LW group (Fig.7), which might serve enough epithelial resources for nascent HF growth. What's more, the higher proportion of interfollicular epidermal basal cell^{2} (IFEB^{2}) and interfollicular epidermal differentiated cell^{2} (IFED^{2}) were observed in the ECM_LW group, supporting more neo-epithelium proliferation in the presence of scaffolds. Increased epithelialization in large wound healing with implanted scaffold was confirmed in IF staining of Krt5 and Krt10 (Fig.6K).

Subclustering of neutrophil

Firstly, activated by platelets, neutrophils are the first responding immune cells acting as the critical mediators of innate immune system. They are necessary for the degradation of biomaterials as well as recruitment and differentiation of monocytes(*23*). Four neutrophil subsets including Il1b^{+}Retnlg^{+} peripheral blood neutrophil (PBN^{2}), Il1a^{+}Tnf^{+} neutrophil1 (Neu1), Lrg1^{+}Il1r2^{+} neutrophil2 (Neu2), Ccl9^{+}Rgs1^{+} neutrophil3 (Neu3) were identified in our dataset (Fig.S8, A~B). KEGG analysis showed the PBN^{2} was enriched in mitophagy, which was essential for neutrophil differentiation(*24*). Neu1 and Neu2 were respectively related to phagosome and Fc-gamma R mediated phagocytosis. While Neu3 showed gene enrichment in leukocyte migration and Th17 cell differentiation. Neu3 was the only subsets owned a higher proportion in ECM_LW group (Fig.S8 C).

Subclustering of dendritic cell

Dendritic cell (DC) was classified into two subclusters including Krt5^{+}Krt14^{+} langerhans cell (LC) and Cd86^{+} monocyte derived dendritic cell (MDC) (Fig.S8, D~E). KEGG analysis showed that LC and MDC respectively related to phagosome and antigen presentation (Fig.S8 F). There was no obvious difference in the proportion of DC subsets between the two groups.

Subclustering of monocyte and macrophage

Macrophages were of vital importance in orchestrating biomaterial related FBR and tissue regeneration(*25*). Three subsets of macrophages including (Ccl8^{+}Folr2^{+}C1qa^{+}Mrc1^{+}) AIM^{2}, (Mmp12^{+}Arg1^{+}Inhba^{+}Nos2^{+}) PIM^{2} and (Ly6c2^{+}Plac8^{+}Cytip^{+}H2-Eb1^{+}) Mono^{2} were determined. The Ctrl_LW group contributed to a larger proportion of all three subsets, suggesting that the scaffold might play a role in the reduction of macrophage infiltration at the proliferative stage (Fig.8 A~C).

Subclustering of T cell

T cells were the only immune cell which owned a higher proportion in ECM_LW group (Fig.S8 B). Subclustering of T cells resulted in seven subsets (Fig.8 D). In addition to Cd8b1^{+} cytotoxic T cell^{2} (CTL^{2}), (Tyrobp^{+}Nkg7^{+}Xcl^{+}) nature killer cell^{2} (NKT^{2}), (Il17a+Il17f^{+}) T helper17^{2} (Th17^{2}), Foxp3^{+} T regulatory cell^{2} (Treg^{2}), and (Trdv4^{+}Cd7^{+}Ctsw^{+}) γδT cell^{2} (Tγδ^{2}) which had been defined in Fig.3 G, two new immune cell subclusters including (Bcl11a^{+}Id3^{+}Notch1^{+}) innate lymphoid cell (ILC) and (Gata3^{+}Il5^{+}) T helper2 (Th2) cell were identified in our dataset based on published research(*26, 27*). Derived from common lymphoid progenitors, ILCs mirror αβ T cell subtypes functionality responding to local signals but lack antigen-specific receptors. In skin, tissue resident ILCs play key roles in barrier integrity, inflammatory response initiation, and immunological response modulation in wound repairing(*27-30*). Correlation analysis showed that ILC and Th2 were respectively highly correlated with CTL^{2} and Th17^{2} (Fig. 8E). Remarkablely, skin-resident ILC in our dataset possessed a tissue specific transcriptional profile that co-expression genes related to T cell functionality (Cd3d^{+}Klf4^{+}Fst^{+}Itga6^{+}) and HF morphology (Wnt4^{+}Sox9^{+}Fgfr2^{+}). Gene enrichment analysis showed the ILC was related to bacterial invasion of epithelial, leukocyte transendothelial migration as well as hair follicle development (Fig.8, G~H). It was suggested that ILCs might initiate HF neogenesis by balancing reparative and pro-inflammatory function(*31*). Collectively, our dataset suggested that ECM-scaffold exerted the immune-regulatory effect on the further activation of adaptive systems in large wound healing, which might play role in HF development.

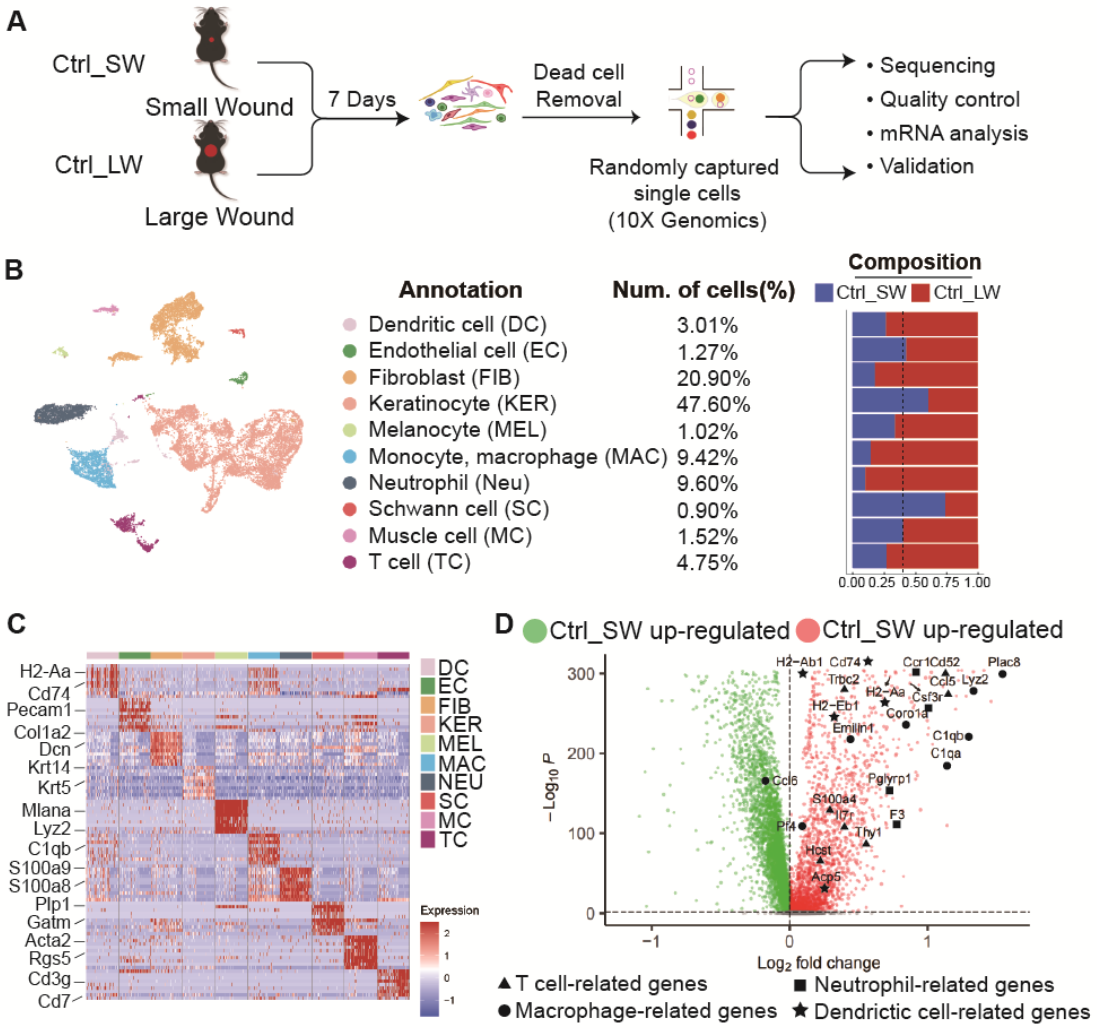

Fig. S1. Overview of the single-cell transcriptome analysis between Ctrl_SW and Ctrl_LW. (A) Single-cell experiment workflow. (B) Cells were categorized into 10 main clusters. The number of cell populations in each cluster, number of cells (%), and composition of Ctrl_SW and Ctrl_LW groups were listed. (C) Heatmap showed top10 marker genes for different clusters. (D) Volcano plot showing interested differentially expressed genes in Ctrl_SW and Ctrl_LW group (scRNA-seq).

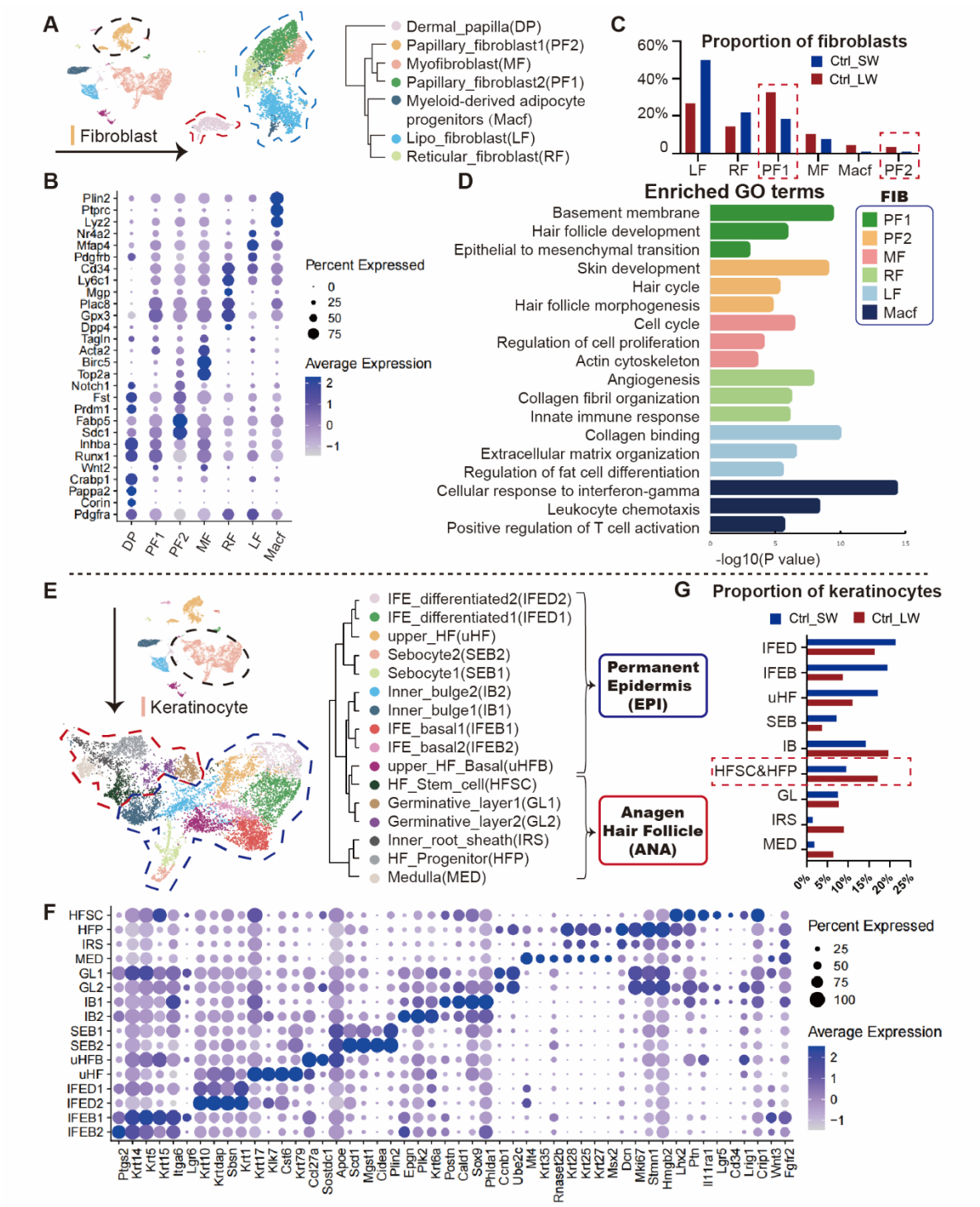

Fig. S2. Further analysis of fibroblasts and keratinocytes between Ctrl_SW and Ctrl_LW. (A) Subclustering of fibroblasts showing 7 subsets and hierarchical clustering of average gene expression using pearson correlation analysis. (B) Marker genes for each fibroblasts subset. (C) Proportion of each subset in two groups. (D) GO enrichment analysis of wound fibroblast

subtypes. (E) Subclustering of keratinocytes showing 16 subsets and hierarchical clustering of average gene expression using pearson correlation analysis. (F) Marker genes for each keratinocytes subset. (G) Proportion of each keratinocytes subset in two groups.

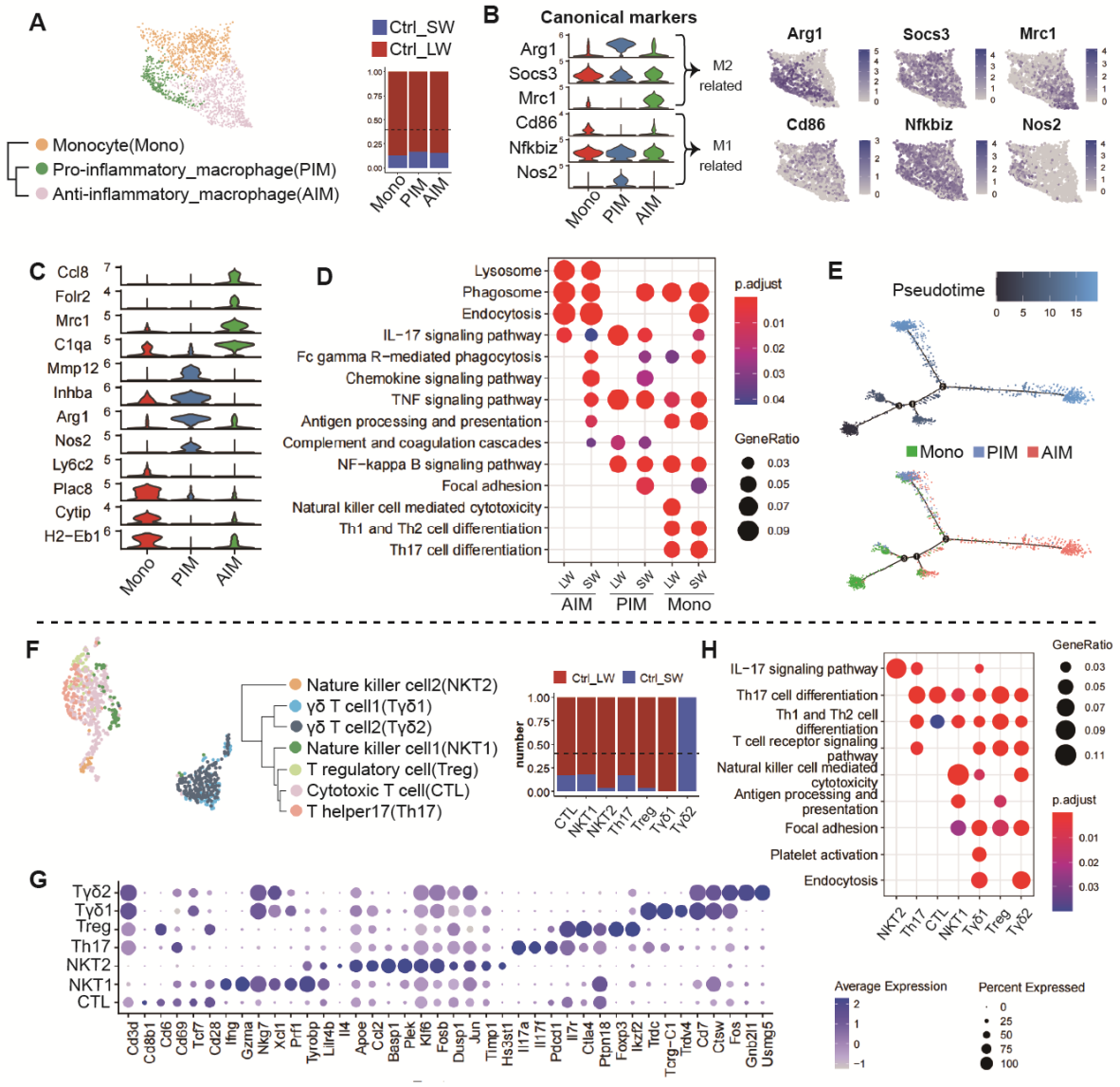

Fig. S3. Analysis of MAC and T cells between Ctrl_SW and Ctrl_LW. (A) Subclustering of MAC showing three subsets and hierarchical clustering of average gene expression (pearson correlation analysis); The composition for each subset. (B) Expression of canonical M1 and M2 markers was inappropriate to identify the subtypes. (C) Marker genes for each MAC subset and (D) gene set enrichment analysis in KEGG pathway. (E) Pseudo-temporal ordering and the distribution of MAC subsets. (F) Subclustering of T cells showing seven subsets and hierarchical clustering of average gene expression (pearson correlation analysis); The composition for each subset. (G) Marker genes for T cell subsets and (H) gene set enrichment analysis in KEGG

pathway.expression using pearson correlation analysis. (F) Marker genes for each keratinocytes subset. (G) Proportion of each keratinocytes subset in two groups.

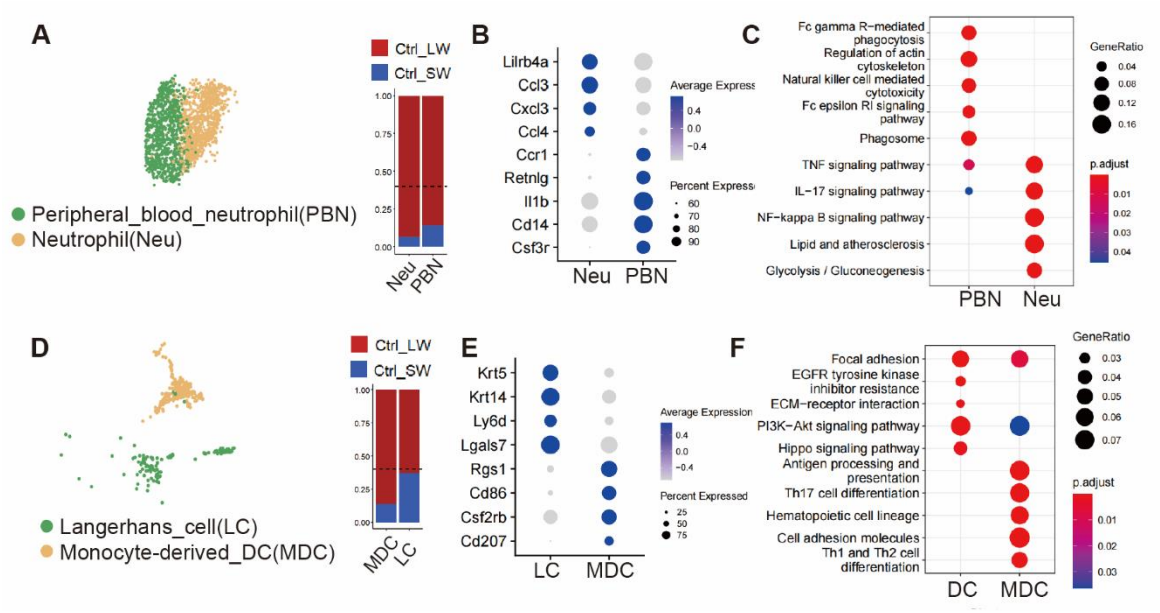

Fig. S4. Further scRNA-seq analysis of neutrophils and dendritic cells between Ctrl_SW and Ctrl_LW. (A) Subclustering of neutrophils showing 2 subsets and the composition for each subset. (B) Marker genes for each neutrophil subset. (C) Gene enrichment analysis of KEGG pathway. (D) Subclustering of dendritic cells showing two subsets and the composition for each subset. (E) Marker genes for each dendritic cell subset. (F) Gene enrichment analysis of KEGG pathway.

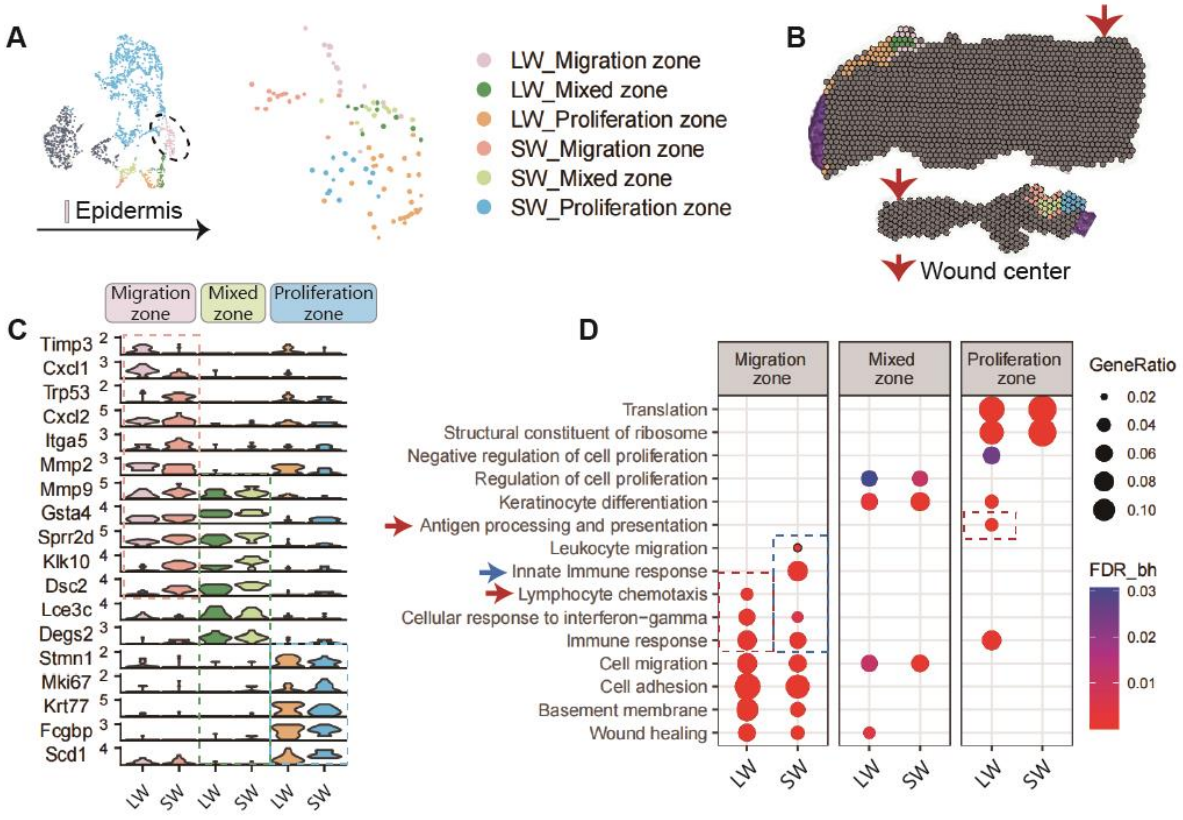

Fig. S5. Further subclustering analysis of epidermis in Ctrl_SW and Ctrl_LW. (A)Subsets of epidermis in each group. (B) Corresponding spatial plot. (C) StackedVlnPlot showed marker genes differentially expressed in each region. (D) Enrichment analysis of GO terms.

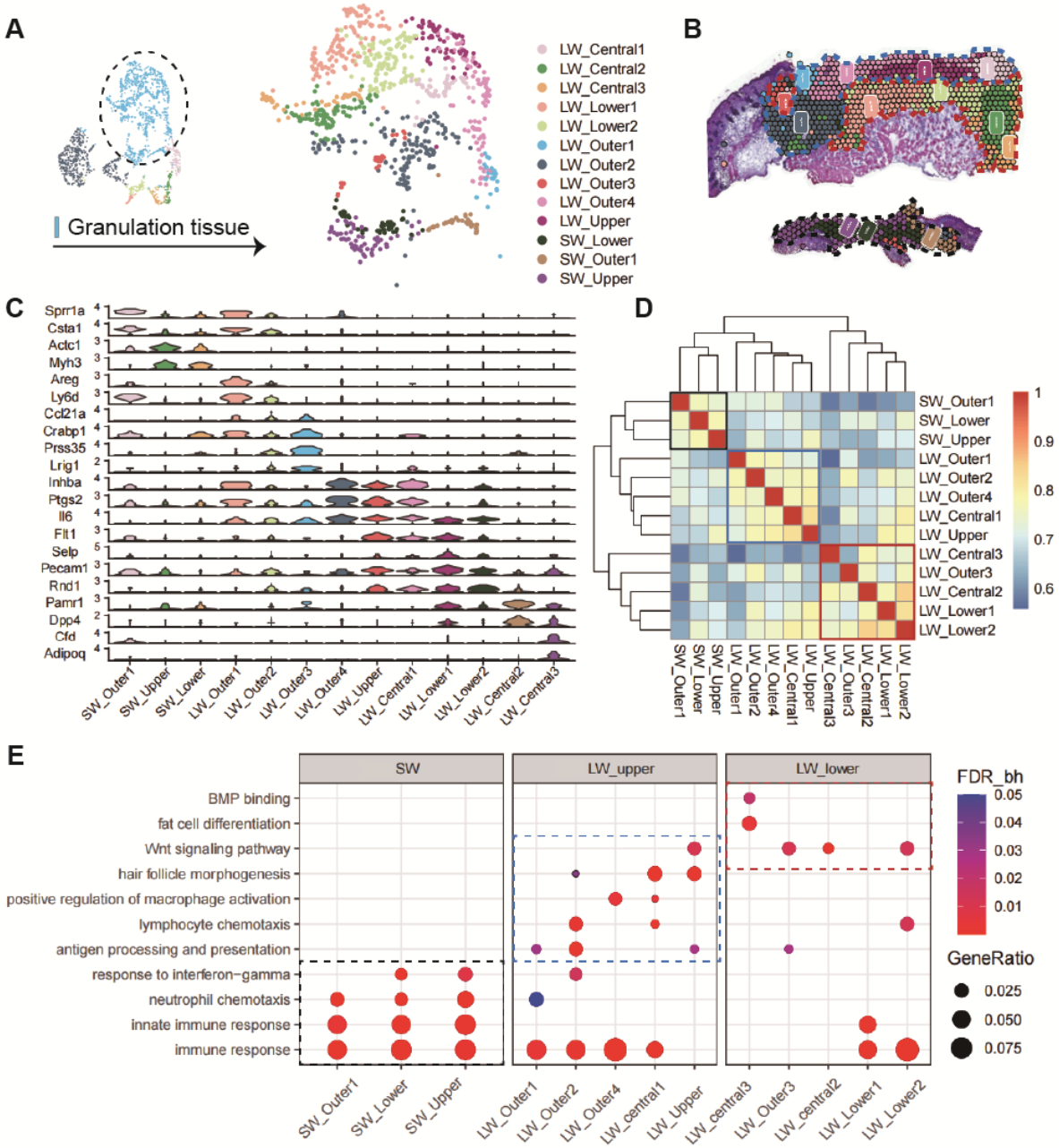

Fig. S6. Further subclustering analysis of granulation tissue in Ctrl_SW and Ctrl_LW.

(A) Subsets of granulation tissue in each group. (B) Corresponding spatial plot of each region. (C) StackedVlnPlot showed marker genes differentially expressed in each region. (D) 13 regions were grouped into three functional clusters by pearson correlation analysis. (E) Enrichment analysis of GO terms.

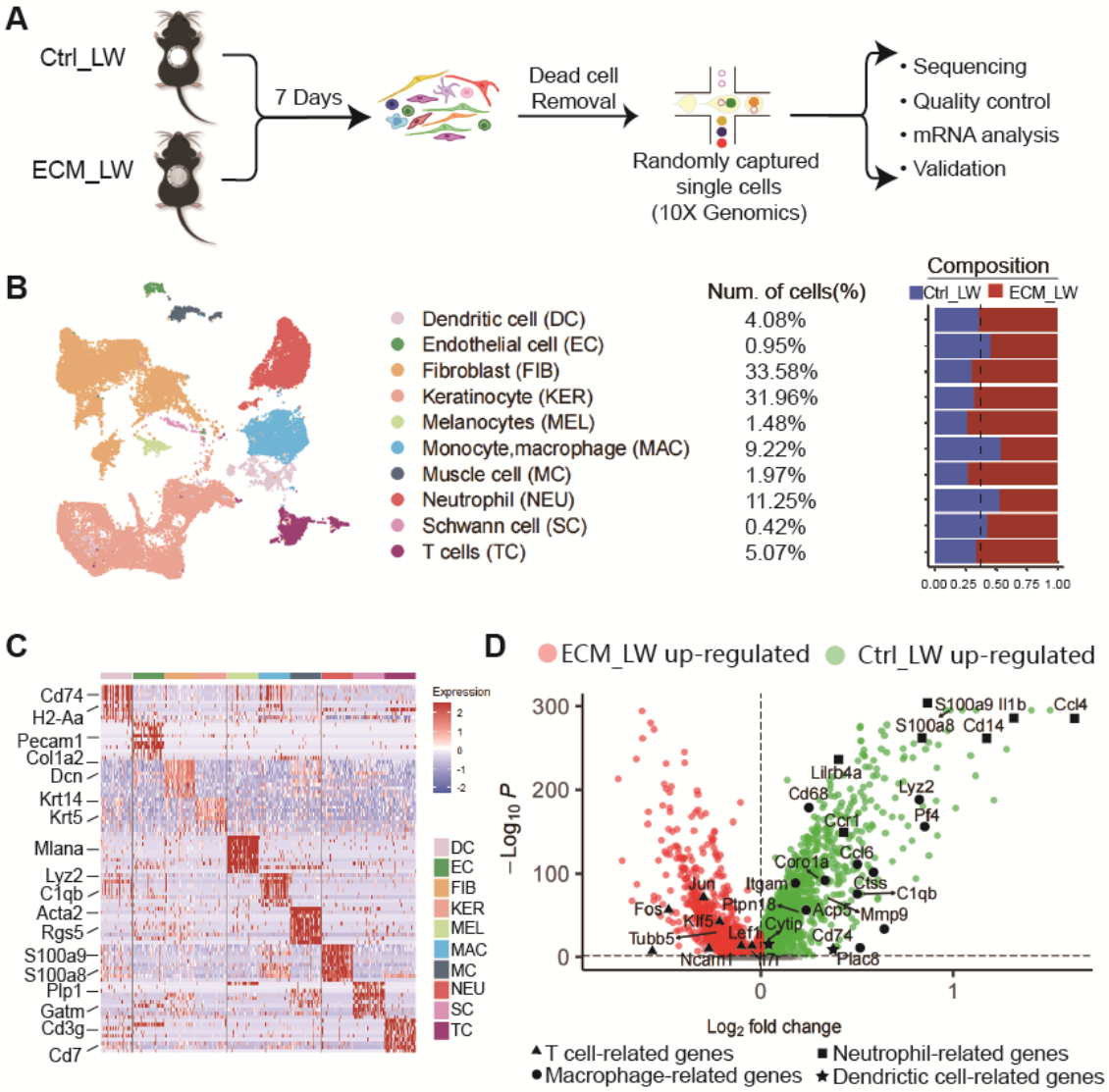

Fig. S7. Overview of the single-cell transcriptome analysis between ECM_LW and Ctrl_LW. (A) Single-cell experiment workflow. (B) Cells were categorized into 10 main clusters. The number of cell populations in each cluster, number of cells (%), and composition of ECM_LW and Ctrl_LW groups were listed. (C) Heatmap showed top10 marker genes for each cluster. (D) Volcano plot showing interested differentially expressed genes in ECM_LW and Ctrl_LW group (scRNA-seq).

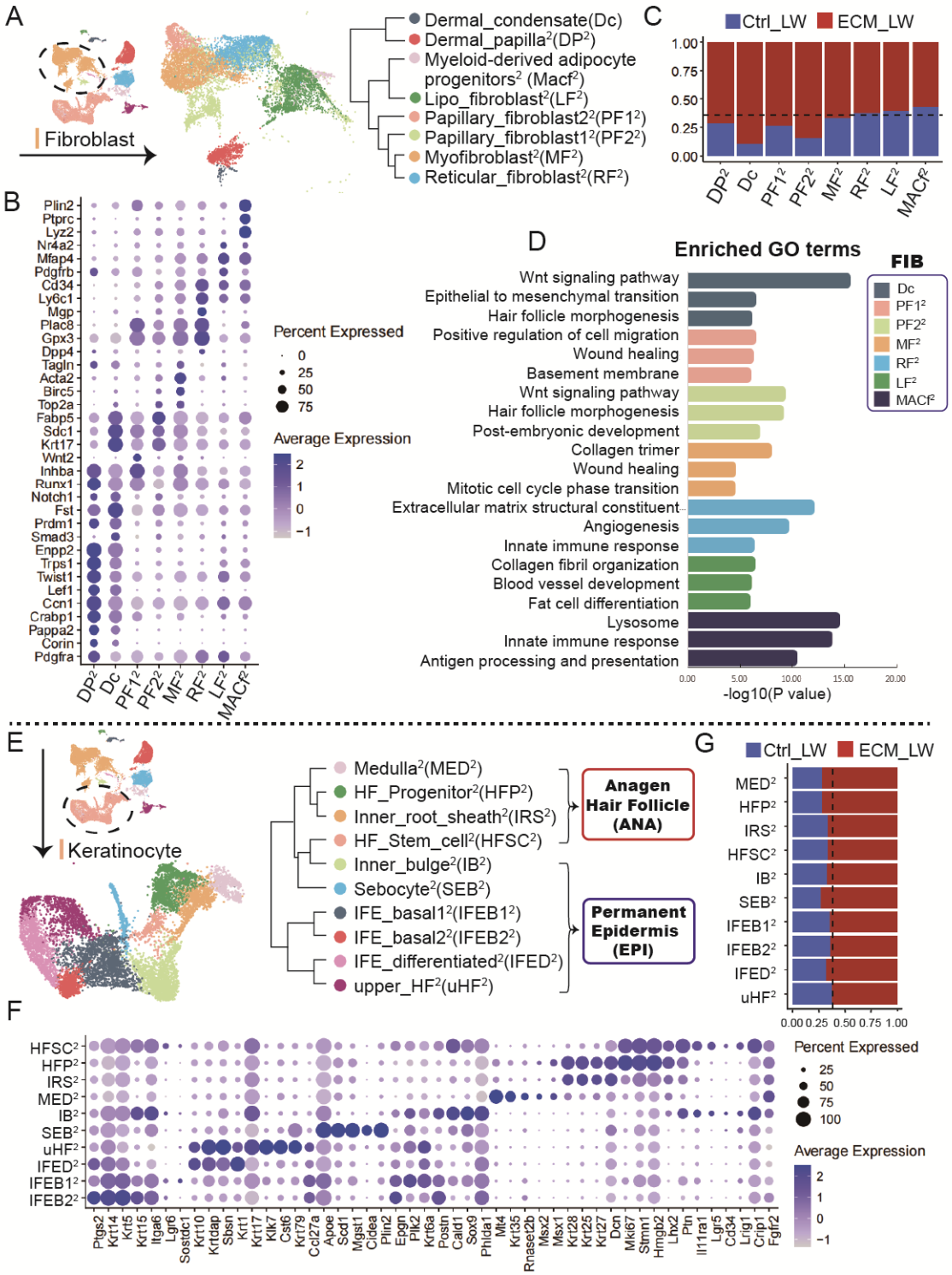

Fig. S8. Further analysis of fibroblasts and keratinocytes between ECM_LW and Ctrl_LW. (A) Subclustering of fibroblasts showing 8 subsets; hierarchical clustering of average gene expression using pearson correlation analysis. (B) Marker genes for each fibroblasts subset. (C)

Proportion of each fibroblast subset in two groups. (D) GO enrichment analysis of wound fibroblast subtypes. (E) Subclustering of keratinocytes showing 10 subsets; hierarchical clustering of average gene expression using pearson correlation analysis. (F) Proportion of each keratinocytes subset in two groups. (G) Marker genes for each keratinocytes subset.

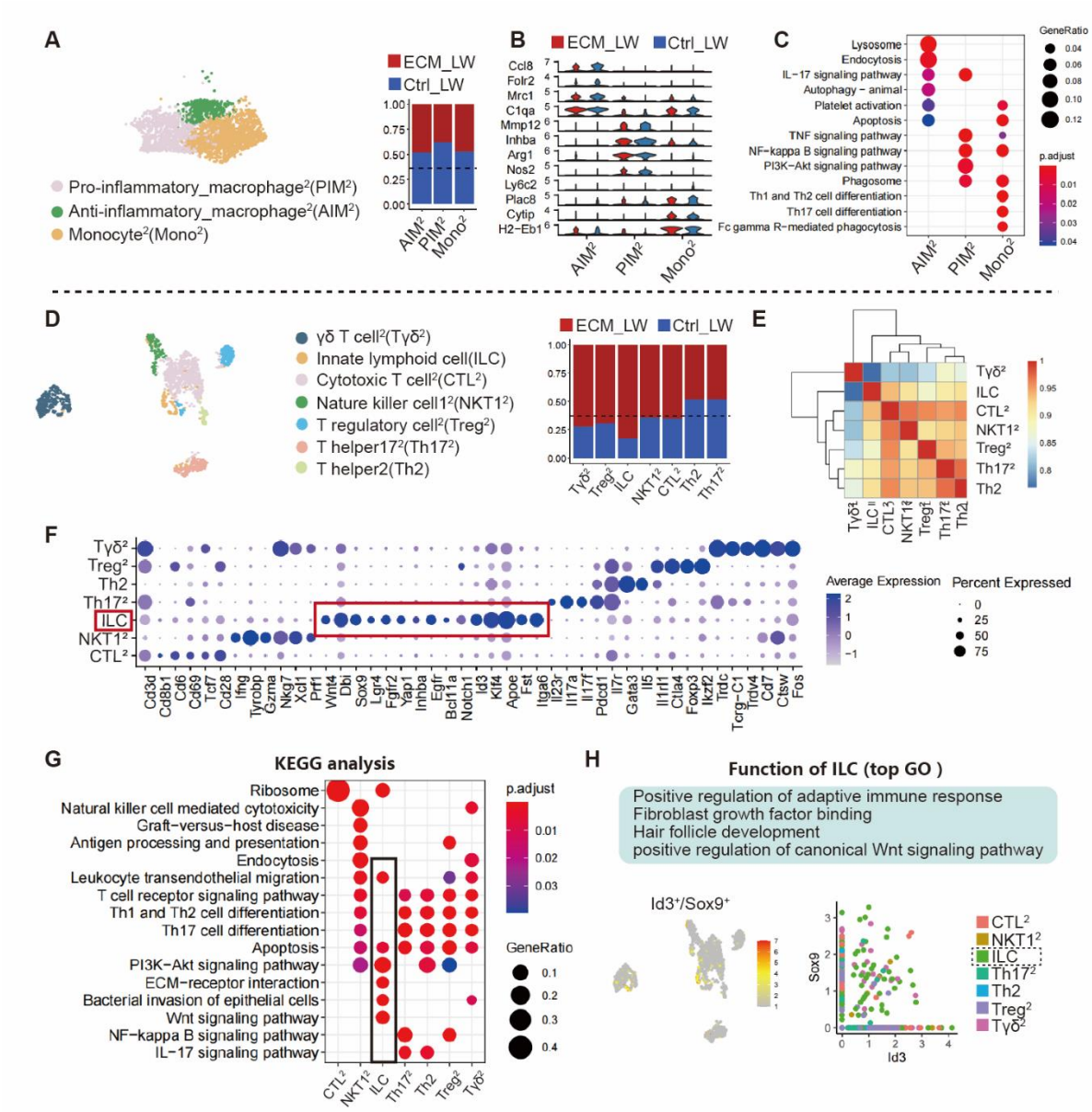

Fig. S9. Analysis of immune cells between ECM_LW and Ctrl_LW. (A) Subclustering of MAC showing three subsets and the composition for each subset. (B) Marker genes for each MAC subset and (C) enrichment analysis in KEGG pathway. (D) Subclustering of T cells showing seven subsets and the composition for each subset. (E) Pearson correlation analysis of T cell subsets based on average gene expression. (F) Marker genes for T cell subsets and (G) enrichment analysis of KEGG pathway. (H) GO enrichment analysis of ILC; Overlay of Id3 and Sox9 expression onto the t-SNE space reveals Id3+/ Sox9+ double-positive subclusters.

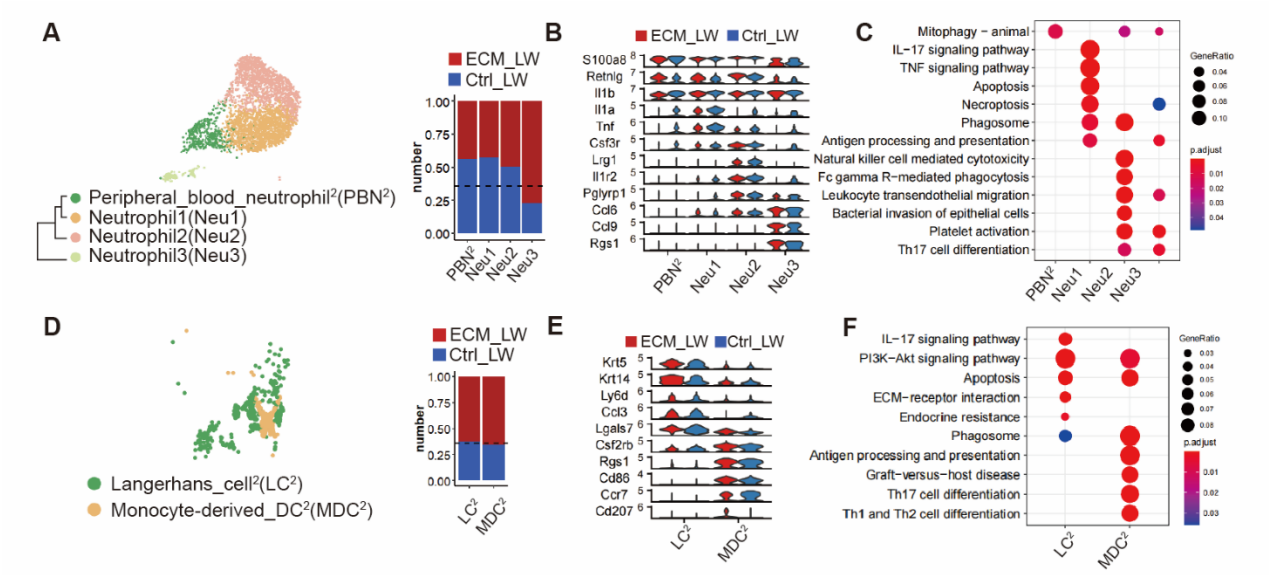

Fig. S10. Subclustering analysis of neutrophils and dendritic cells between ECM_LW and Ctrl_LW. (A) Subclustering of neutrophils showing 4 subsets and hierarchical clustering of average gene expression using pearson correlation analysis. The composition for each subset was listed. (B) Marker genes for each neutrophil subset. (C) Gene enrichment analysis of KEGG pathway. (D) Subclustering of dendritic cells showing two subsets and the composition for each subset was listed. (E) Marker genes for each dendritic cells subset. (F) Gene enrichment analysis of KEGG pathway.

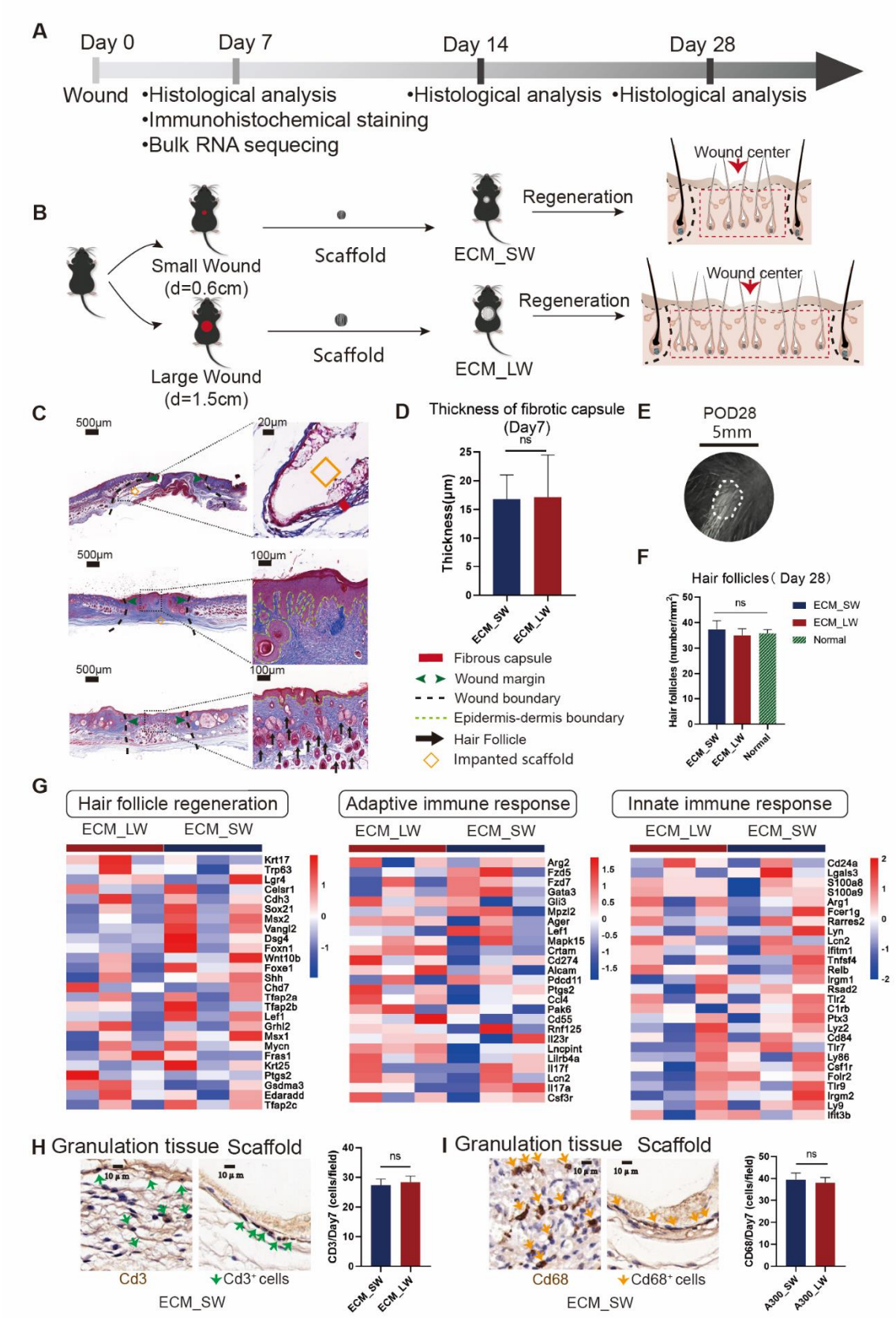
A
Day 0
Day 7
Day 14
Day 28
Wound
•Histological analysis
•Immunohistochemical staining
•Bulk RNA sequecing
•Histological analysis
•Histological analysis
B
Small Wound
(d=0.6cm)
Large Wound
(d=1.5cm)
Scaffold
Scaffold
ECM_SW
ECM_LW
Regeneration
Regeneration
Wound center
Wound center
C
500μm
20μm
500μm
100μm
500μm
100μm
D
Thickness of fibrotic capsule
(Day7)
ns
Thickness(μm)
ECM_SW
ECM_LW
Fibrous capsule
Wound margin
Wound boundary
Epidermis-dermis boundary
Hair Follicle
Impanted scaffold
E
POD28
5mm
F
Hair follicles（Day 28）
ns
Hair follicles (number/mm²)
ECM_SW
ECM_LW
Normal
G
Hair follicle regeneration
Adaptive immune response
Innate immune response
ECM_LW
ECM_SW
Krt17
Trp63
Lgr4
Celsr1
Cdh3
Sox21
Msx2
Vangl2
Dsg4
Foxn1
Wnt10b
Foxe1
Shh
Chd7
Tfap2a
Tfap2b
Lef1
Grhl2
Msx1
Mycn
Fras1
Krt25
Ptgs2
Gsdma3
Edaradd
Tfap2c
Arg2
Fzd5
Fzd7
Gata3
Gli3
Mpzl2
Ager
Lef1
Mapk15
Crtam
Cd274
Alcam
Pdcd11
Ptgs2
Ccl4
Pak6
Cd55
Rnf125
Il23r
Lncpint
Llrb4a
Il17f
Lcn2
Il17a
Csf3r
Cd24a
Lgals3
S100a8
S100a9
Arg1
Fcer1g
Rarres2
Lyn
Lcn2
Ifitm1
Tnfsf4
Relb
Irgm1
Rsad2
Tlr2
C1rb
Ptx3
Lyz2
Cd84
Tlr7
Ly86
Csf1r
Folr2
Tlr9
Irgm2
Ly9
Ifit3b
H Granulation tissue Scaffold
10 μm
Cd3
Cd3⁺ cells
ECM_SW
CD3/Day7 (cells/field)
ns
ECM_SW
ECM_LW
I Granulation tissue Scaffold
10 μm
Cd68
Cd68⁺ cells
ECM_SW
CD68/Day7 (cells/field)
ns
A300_SW
A300_LW

Fig. S11. Evaluation of the healing of small and large full-thickness wound with implanted ECM scaffolds. (A) Workflow for evaluating skin wound healing. (B) Surgical process for skin excisional wound model of ECM_SW and ECM_LW group. (C) MST staining of ECM_SW samples. (D) Thickness of fibrotic capsule around membrane of ECM_SW and ECM_LW group. (E) Gross photograph of small wound treated with scaffold on POD28. (F) Histologic quantification of de novo hair follicles on POD28. (G) Heatmap showing expression of hair follicle regeneration, adaptive immune response, and innate immune response related genes. (H) IHC staining of Cd3 in ECM_SW sample and comparison of CD3+ cellular infiltration between ECM_SW and ECM_LW. (I) IHC staining of Cd68 in ECM_SW sample and comparison of CD68+ cellular infiltration between ECM_SW and ECM_LW.

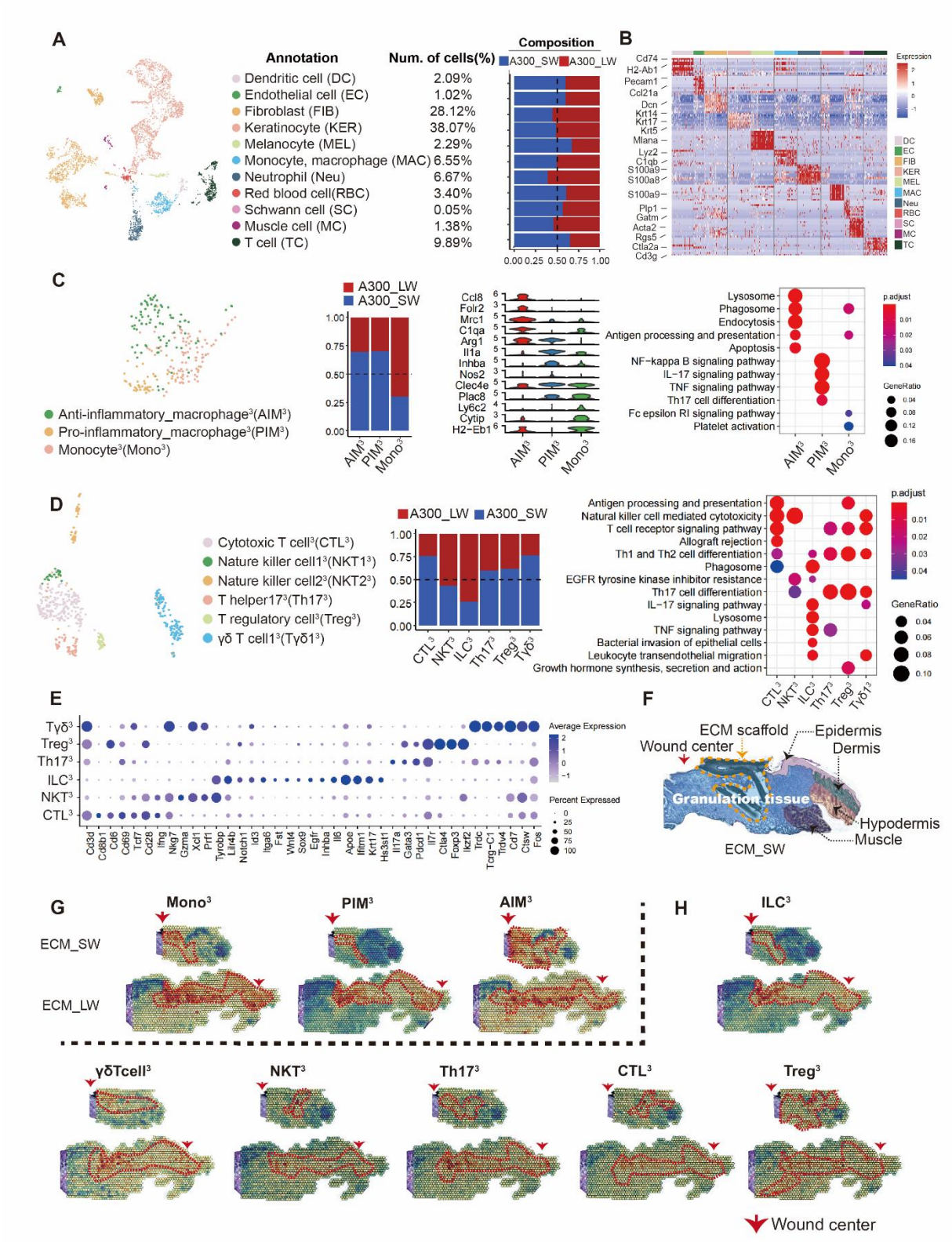

Fig. S12. ScRNA-seq and ST analysis between ECM_SW and ECM_LW. (A) Single cells were categorized into 11 main clusters. The number of cell populations in each cluster, number

of cells (%), and composition of ECM_LW and ECM_SW groups were listed. Heatmap and top10 marker genes for each cluster. (C) Subclustering of MAC showing three subsets; The composition for each subset was listed; Marker genes for each MAC subset and enrichment analysis of KEGG pathway. (D) Subclustering of T cells showing seven subsets; The composition for each subset was listed and enrichment analysis of KEGG analysis. (E) Marker genes for T cell subsets. (F) The annotations indicated the anatomical structures of ECM_SW sample. Spatial feature plots showed defined MAC (G) and T cells subclusters (H) distribution using Addmodulescore.

1. C. Wang *et al.*, The diameter factor of aligned membranes facilitates wound healing by promoting epithelialization in an immune way. *Bioactive materials* **11**, 206-217 (2022).doi:10.1016/j.bioactmat.2021.09.022
2. C. Hu *et al.*, Dissecting the microenvironment around biosynthetic scaffolds in murine skin wound healing. *Science advances* **7**, (2021).doi:10.1126/sciadv.abf0787
3. R. R. Driskell *et al.*, Distinct fibroblast lineages determine dermal architecture in skin development and repair. *Nature* **504**, 277-281 (2013).doi:10.1038/nature12783
4. S. Abbasi *et al.*, Distinct Regulatory Programs Control the Latent Regenerative Potential of Dermal Fibroblasts during Wound Healing. *Cell stem cell* **27**, 396-412.e396 (2020).doi:10.1016/j.stem.2020.07.008
5. B. A. Shook *et al.*, Myofibroblast proliferation and heterogeneity are supported by macrophages during skin repair. *Science (New York, N.Y.)* **362**, (2018).doi:10.1126/science.aar2971
6. C. F. Guerrero-Juarez *et al.*, Single-cell analysis reveals fibroblast heterogeneity and myeloid-derived adipocyte progenitors in murine skin wounds. *Nature communications* **10**, 650 (2019).doi:10.1038/s41467-018-08247-x
7. B. A. Shook *et al.*, Dermal Adipocyte Lipolysis and Myofibroblast Conversion Are Required for Efficient Skin Repair. *Cell stem cell* **26**, 880-895.e886 (2020).doi:10.1016/j.stem.2020.03.013
8. S. Joost *et al.*, The Molecular Anatomy of Mouse Skin during Hair Growth and Rest. *Cell stem cell* **26**, 441-457.e447 (2020).doi:10.1016/j.stem.2020.01.012
9. S. Joost *et al.*, Single-Cell Transcriptomics Reveals that Differentiation and Spatial Signatures Shape Epidermal and Hair Follicle Heterogeneity. *Cell systems* **3**, 221-237.e229 (2016).doi:10.1016/j.cels.2016.08.010
10. D. Haensel *et al.*, Defining Epidermal Basal Cell States during Skin Homeostasis and Wound Healing Using Single-Cell Transcriptomics. *Cell reports* **30**, 3932-3947.e3936 (2020).doi:10.1016/j.celrep.2020.02.091
11. M. W. Hughes *et al.*, Msx2 Supports Epidermal Competency during Wound-Induced Hair Follicle Neogenesis. *The Journal of investigative dermatology* **138**, 2041-2050 (2018).doi:10.1016/j.jid.2018.02.043

12. X. Wang *et al.*, Macrophages induce AKT/β-catenin-dependent Lgr5(+) stem cell activation and hair follicle regeneration through TNF. *Nature communications* **8**, 14091 (2017).doi:10.1038/ncomms14091
13. T. A. Wynn, K. M. Vannella, Macrophages in Tissue Repair, Regeneration, and Fibrosis. *Immunity* **44**, 450-462 (2016).doi:10.1016/j.immuni.2016.02.015
14. K. Sadtler *et al.*, Design, clinical translation and immunological response of biomaterials in regenerative medicine. *Nature Reviews Materials* **1**, 16040 (2016).doi:10.1038/natrevmats.2016.40
15. K. Sadtler *et al.*, Developing a pro-regenerative biomaterial scaffold microenvironment requires T helper 2 cells. *Science (New York, N.Y.)* **352**, 366-370 (2016).doi:10.1126/science.aad9272
16. D. Gay *et al.*, Fgf9 from dermal γδ T cells induces hair follicle neogenesis after wounding. *Nature medicine* **19**, 916-923 (2013).doi:10.1038/nm.3181
17. P. Lee *et al.*, Stimulation of hair follicle stem cell proliferation through an IL-1 dependent activation of γδT-cells. *eLife* **6**, (2017).doi:10.7554/eLife.28875
18. A. Bassez *et al.*, A single-cell map of intratumoral changes during anti-PD1 treatment of patients with breast cancer. *Nature medicine* **27**, 820-832 (2021).doi:10.1038/s41591-021-01323-8
19. B. Z. Qian *et al.*, CCL2 recruits inflammatory monocytes to facilitate breast-tumour metastasis. *Nature* **475**, 222-225 (2012)
20. I. C. Boothby, J. N. Cohen, M. D. Rosenblum, Regulatory T cells in skin injury: At the crossroads of tolerance and tissue repair. *Science immunology* **5**, (2020).doi:10.1126/sciimmunol.aaz9631
21. K. Mok *et al.*, Dermal Condensate Niche Fate Specification Occurs Prior to Formation and Is Placode Progenitor Dependent. *Developmental cell* **48**, 32-48.e35 (2019).doi:10.1016/j.devcel.2018.11.034
22. D. Kim *et al.*, Noncoding dsRNA induces retinoic acid synthesis to stimulate hair follicle regeneration via TLR3. *Nature communications* **10**, 2811 (2019).doi:10.1038/s41467-019-10811-y
23. B. O. Ode Boni, L. Lamboni, T. Souho, M. Gauthier, G. Yang, Immunomodulation and cellular response to biomaterials: the overriding role of neutrophils in healing. *Materials Horizons* **6**, 1122-1137 (2019).doi:10.1039/C9MH00291J
24. T. Riffelmacher *et al.*, Autophagy-Dependent Generation of Free Fatty Acids Is Critical for Normal Neutrophil Differentiation. *Immunity* **47**, 466-480.e465 (2017).doi:10.1016/j.immuni.2017.08.005
25. C. Chu *et al.*, Modulation of foreign body reaction and macrophage phenotypes concerning microenvironment. *Journal of biomedical materials research. Part A* **108**, 127-135 (2020).doi:10.1002/jbm.a.36798
26. Y. Yu *et al.*, Single-cell RNA-seq identifies a PD-1(hi) ILC progenitor and defines its development pathway. *Nature* **539**, 102-106 (2016).doi:10.1038/nature20105
27. P. Bielecki *et al.*, Skin-resident innate lymphoid cells converge on a pathogenic effector state. *Nature* **592**, 128-132 (2021).doi:10.1038/s41586-021-03188-w
28. H. Y. Shih *et al.*, Developmental Acquisition of Regulomes Underlies Innate Lymphoid Cell Functionality. *Cell* **165**, 1120-1133 (2016).doi:10.1016/j.cell.2016.04.029
29. Z. Li *et al.*, Epidermal Notch1 recruits RORγ(+) group 3 innate lymphoid cells to orchestrate normal skin repair. *Nature communications* **7**, 11394 (2016).doi:10.1038/ncomms11394

30. M. Ebbo, A. Crinier, F. Vély, E. Vivier, Innate lymphoid cells: major players in inflammatory diseases. *Nature reviews. Immunology* **17**, 665-678 (2017).doi:10.1038/nri.2017.86
31. D. T. Chang, E. Colton, J. M. Anderson, Paracrine and juxtacrine lymphocyte enhancement of adherent macrophage and foreign body giant cell activation. *Journal of biomedical materials research. Part A* **89**, 490-498 (2009).doi:10.1002/jbm.a.31981